University of Nevada, Reno

Development and Evaluation of a Real-Time Mid-Infrared Photoacoustic Spectrometer for Measuring Silica and Other Mineral Dust Mass Concentrations

A thesis submitted in partial fulfillment of the

requirements for the degree of Master of Science in

Atmospheric Science

By

Samuel Taylor

W. Patrick Arnott/Thesis Advisor

August, 2021

THE GRADUATE SCHOOL

We recommend that the thesis
prepared under our supervision by

SAMUEL JOE TAYLOR

Entitled

Development and Evaluation of a Real-Time Mid-Infrared Photoacoustic Spectrometer for Measuring Silica and Other Mineral Dust Mass Concentrations

be accepted in partial fulfillment of the
requirements for the degree of

MASTER OF SCIENCE

W. Patrick Arnott, Ph.D.
Advisor

Xiaoliang Wang, Ph.D.
Committee Member

Karoly Kocsis, Ph.D.
Graduate School Rep.

David W. Zeh, Ph.D., Dean
Graduate School

August, 2021

Abstract

Respirable crystalline silica (RCS) continues to be a major health concern for those employed in the mining industry. While there have been improvements in the turn-around time for filter-based measurements of RCS in mine environments, there is a distinct lack of a real-time method for quantifying it. In this study, a new real-time method using photoacoustic spectroscopy with an infrared tunable quantum cascade laser was developed. The most useful spectral region was found to be between 11 μm and 13 μm, and the wavelength for airborne RCS quantification was determined to be 12.495 μm. It was also found that the instrument is capable of accounting for, and quantifying, kaolinite, and coal dust, which are also commonly found in coal mines. A Sensirion SPS30 low-cost air quality sensor was used to monitor particulate matter concentrations, while a TSI Aerodynamic Particle Sizer (APS) was used to record size distributions. The accuracy of this method was determined by comparing the results to the NIOSH filter-based FTIR technique for RCS mass concentration measurement. The filter-based FTIR technique, SPS30, and photoacoustic spectrometer measurements are shown to correlate strongly. The new instrument will also be useful for measuring aerosol light absorption by windblown dust in the thermal infrared atmospheric window.

Dedication

This work is dedicated to all of the people who have helped me and believed in me throughout my education and my life. The results presented herein are the direct culmination of their hopes for me and my continued efforts thanks to them. To my friends and family, particularly to my parents, **Joe Taylor** and **Julie Taylor**, I give my deepest, most heartfelt thanks for supporting me and encouraging me to strive ever higher. My words do you no justice; I wouldn't be where I am today were I not able to lean on you. Thank you for always being here for me.

Acknowledgements

I would like to acknowledge and convey my deepest appreciation and thanks to my advisor, **Dr. W. Patrick Arnott**, for assisting and teaching me as I progressed all of these years. You made learning fun and interesting, and my completion of this degree would not be possible without you as my fountain of knowledge. I would also like to thank my committee members, **Dr. Karoly Charles Kocsis** and **Dr. Xiaoliang Wang**, for their support and input through my graduate education. Additionally, I would like to thank **Pedro Nascimento** for being an excellent coworker and friend throughout our research together. I thoroughly enjoyed learning with you as we spent time together in the lab. Finally, I would like to acknowledge and thank the **National Institute for Occupational Safety and Health** for providing the funding for the project "Development of a Personal Real-Time Respirable Coal Dust and Silica Dust Monitoring Instrument Based on Photoacoustic Spectroscopy," of which this thesis is a direct result.

Contents

List of Figures

List of Equations

Chapter 1: Introduction

1.1 Nature of the RCS Health Hazard in Mining and Industry

Coal mining is a substantial industry employing many workers around the world. Due to the nature of the industry, coal miners are frequently exposed to elevated concentrations of airborne RCS. The medical conditions associated with overexposure to airborne silica and coal dust include pneumoconiosis, emphysema, silicosis, and chronic obstructive pulmonary disease, all of which are known to contribute to "black lung" and other chronic lung diseases. (MSHA, 2010). This respirable health hazard can have a truly overwhelming effect upon the life of a coal worker, sometimes leading even to premature death. Respirable coal dust consists of airborne particles of coal, silica, other minerals, and various types of organic material generated by mining activities. The particles of interest are 4.0 μm in diameter and smaller. The reason for this is because particles that fall within these parameters can be easily inhaled into the deepest parts of the lung, damaging lung function by embedding into and destroying alveoli, a critical structure allowing the transfer of oxygen into the bloodstream (MSHA, 2014). This can have a very harmful and long-lasting effect on the lungs because the body has very few means of removing hazardous material of this size from this region. Studies show that the prevalence rate of lung disease among US coal miners continues to be a problem (Harris, McMurry, & Caughron, 2021; NIOSH, 2011; Reynolds & Jerome, 2021). The effects of

silicosis and other forms of chronic lung disease brought on by exposure to RCS are felt in many other fields as well (Reynolds & Jerome, 2021). Therefore, it is important to monitor RCS concentrations in mining environments in order to prevent the exposure of miners to high concentrations and avoid future health problems.

1.2 Current methods of monitoring silica

Currently, there are three primary methods for monitoring silica and coal dust: (1) NIOSH 7500, 7601, 7603 techniques, (2) Personal dust monitoring that provides dust concentration readings in a near-continuous manner, and (3) A field-based method using an on-site Fourier-Transform Infrared Spectrometer (FTIR).

The most well-known method for monitoring RCS in mining environments comprise the NIOSH 7500, 7601, and 7603 techniques. These techniques involve the offsite preparation of samples via ashing or dissolution of the filter to remove interfering materials, followed by redeposition onto a new filter (Hart et al., 2018). Due to the shipping, preparation, and calculation time needed for these methods, it often takes anywhere from 1 to 2 weeks for the dust concentration results to be posted to the mine site. This comes with the obvious drawback of severe lag time between exposure to potentially hazardous levels of RCS and alerting the exposed individuals. Additionally, because the techniques are filter-based methods, the measurement time typically occurs over the course of about 8 hours. In this case, all that can be known is the time-weighted

average RCS concentration (Hart et al., 2018). So, while effective at determining RCS concentrations over the sampling period, this method has the drawback of being slow and costly in the long run due to sample shipping and filter replacements. In addition, due to time-weighted average concentration measurements, the short-term, elevated dust concentrations in the production areas and throughout the mine cannot be identified.

The Continuous Personal Dust Monitor (CPDM), namely the PDM3700 sold by Thermo-Scientific, is an instrument that provides 30-minute averages of total airborne pollutant concentrations within the respirable diameter range (0.5 to 4.0 microns). The PDM3700 uses a tapered element oscillating microbalance to measure the concentration of airborne particulate matter (MSHA, 2014). Coupling this device with a cyclone designed to sort particles into the desired size ranges allows for accurate measurement of PM_4 (particulate matter mass concentration of 4 microns in diameter or smaller). However, there is a drawback to this method. The device cannot discern between coal dust, silica dust, and other types of material present in the atmosphere and instead only gives a concentration of the total airborne particulate matter (Pampena, Cauda, Chubb, & Meadows, 2020). Due to its tapered oscillating filter system, the unit can get easily damaged every time the filter is changed, as there is a risk of breaking the oscillating element. Breaking this element renders the unit inoperative until the oscillating element is replaced, which can be expensive and time consuming. Additionally, this instrument is

not a “true” real-time monitoring unit, as it can only measure cumulative mass concentrations over a certain period.

Recently, NIOSH has developed a field-based method for measuring respirable silica concentrations to combat the 1 to 2 weeks wait time for dust concentration data. While it is not a real time method, it provides a way to determine RCS concentrations at mine sites immediately after the end of a work shift. An air sampling system made up of a personal sampling pump, a PM_4 cyclone, and a dust sampling cassette is used to collect airborne dust onto a PVC filter throughout a miner’s shift. Once the miner’s shift has ended, the sampled filter is removed for analysis. An onsite Fourier-Transform Infrared Spectrometer (FTIR) capable of evaluating the filter sample over a spectral range of 4000-400 cm^{-1} and a resolution of 4 cm^{-1} is required (Pampena et al., 2020). First, a clean, non-sampled filter from the same group as the sampled filter is analyzed in the FTIR, along with the blank sampled filter. This is done to provide a background transmittance that can be used as a reference for the sampled filter transmittance. The results consist of two files containing the transmittance data from the non-sampled filter and the sampled filter, and their ratio is the transmittance due to the aerosol on the filter. For determining the concentration of RCS during the shift, NIOSH has created and made public their software known as the NIOSH Field Analysis of Silica Tool (FAST). The software receives data from a FTIR spectroscopy instrument and translates it into a silica mass and a silica concentration for respirable dust samples based on the values of sampling time, pump

flow rate, and FTIR transmission spectra through the sampled filter (Pampena et al., 2020). After generating the spectra and carrying out the analysis of the samples, the FAST software requires a file to be read into it with the following fields: sample name, Q, K, M, D, and C. The last five fields are variables generated by the analysis in the FTIR instrument and represent integration areas of a transmission spectrum of a single sample. Each variable represents a different mineral with a signature feature in the sample's spectrum. Q is related to the signature feature of quartz, K is related to kaolinite, M represents microcline, C is related to calcite, and D to dolomite, according to the NIOSH FAST manual. Even though this method is a strong improvement upon silica measuring techniques, it is still not a real time method for silica mass concentration monitoring. As a result, it presents similar problems to the NIOSH 7500, 7601, and 7603 methods.

All of these techniques are useful in monitoring RCS at surface and underground mines, but they each have their drawbacks as well. The need for a simple, real-time instrument to accurately measure RCS is critical. The instrument discussed in chapter and chapter 3 is capable of measuring airborne silica concentrations in real time without the need for deposition on a filter.

Chapter 1 has introduced the problems needed to be addressed and the trajectory by which these issues can be explored. Chapter 2 lays out the theory behind this thesis. It is currently in review for publishing by the Society of Mining Engineers. Chapter 3 addresses the development of the photoacoustic instrument, as well as the additional

resources, instruments, and techniques used to assess the photoacoustic instrument's capabilities. Some of the information found there has been published previously (Nascimento et al., 2021). Chapter 4 shows the resulting data collected from experiments with the photoacoustic instrument and how it compares to different instruments, measurement techniques, and standards. Finally, Chapter 5 addresses the primary conclusions from this study.

Chapter 2: Theory

2.1 Quantum Cascade Lasers

Lasers have been a staple in many scientific fields and research since their invention. They are incredibly useful due to the way they produce high-intensity light at very specific wavelengths that behaves in predictable, manipulatable ways. However, some wavelengths of light are easier to produce than others. While some gas lasers are capable of a high-power output at specific wavelengths in the infrared, tunable mid-to-far infrared lasers have especially been difficult to create. However, with the discovery of quantum tunneling and the invention of superlattices, these lasers became a possibility. Still, the discovery and use of quantum cascade laser (QCL) technology wouldn't become known until 1994, when F. Capasso et al. showed it was viable (Capasso, Faist, Sirtori, & Cho, 1997).

QCLs are a type of semiconductor laser. In semiconductor lasers, there is typically a crystal semiconductor that makes up the active region of the laser. However, within a QCL, the semiconductor is instead replaced with a superlattice, a type of semiconductor typically made up of alternating layers of indium gallium arsenide and aluminum gallium arsenide, which are only several nanometers thick (Capasso et al., 1997). Because the layers are quantum-sized, the superlattice forms a series of quantum wells at different potentials to each other. Electrons that are stable in one well can travel to another well of different potential through a process called quantum tunneling. When this occurs within the superlattice and the electron arrives within a well where its energy state is no longer stable, it will decay to the next state that is stable, a process known as an intersubband transition (Capasso et al., 1997). During its decay, the electron will give off a photon. These photons are then columnated into the IR laser beam.

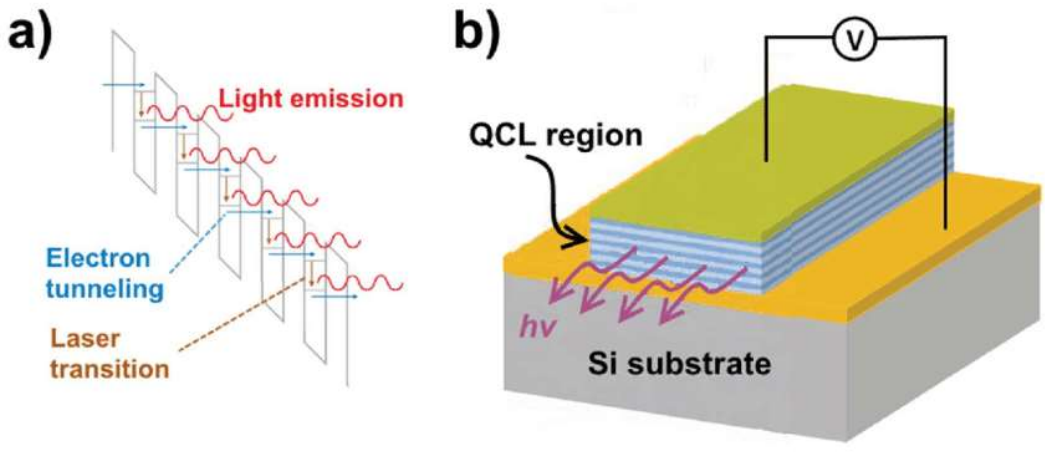

Figure 1: QCL electron cascade example. (Grzela, 2015)

When a QCL is referred to as “tunable,” this indicates that the device can produce different wavelengths within a spectral range. Depending on the wavelengths being produced and the power output of the laser, different spectral ranges are possible. QCLs have already been shown to be useful for absorption spectroscopy (Curl et al., 2010; Namjou et al., 1998). A tunable QCL would be able to scan through a spectral range and, when coupled with the photoacoustic instrument as described below, allow for the generation of aerosol spectra.

2.2 Real Time Measurements of Aerosol Light Absorption

First, a review of the relevant terminology and concepts underlying the method provides a framework for the discussion in this manuscript. Figure 2 illustrates the basic interactions of light and dust aerosol.

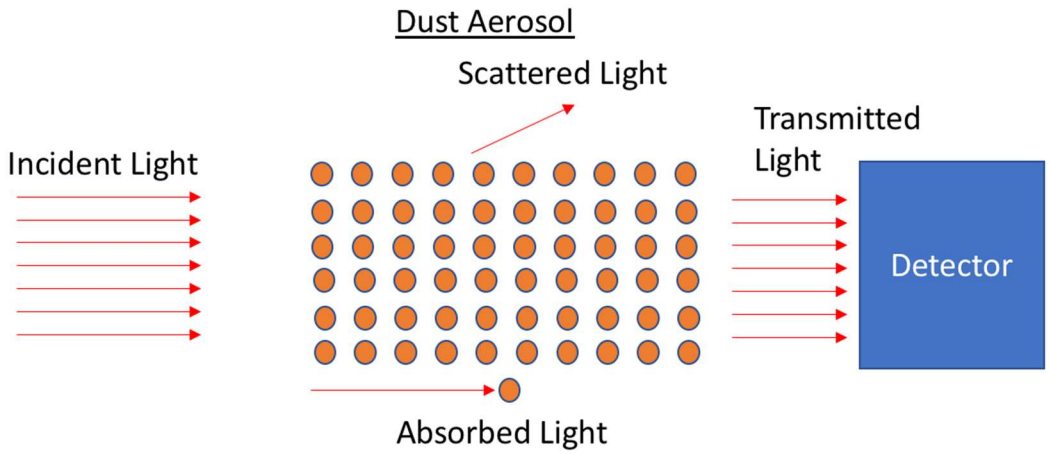

Figure 2: An example of aerosol light absorption. Interaction of light and dust aerosol – possibly a complex mixture of coal, SiO_2 and kaolinite. In practice, the dust is not arranged in a regular array as shown here but is randomly distributed within the chamber.

Light is incident on a plume of dust aerosol, and portions of the light are scattered, absorbed, and transmitted to the detector. Absorbed light heats the aerosol, while scattered light is available for further interactions with the dust plume. The photoacoustic instrument described below (K. Lewis, Arnott, Moosmuller, & Wold, 2008) directly measures detected portions for freely suspended aerosol (no filters are used), and the transmitted light is used to calibrate these measurements (Gyawali et al., 2012). The NIOSH spectroscopic filter-based method being used for end-of-shift detection of silicate dust aerosol deposited on filters involves the additional interaction of a light-aerosol-filter-detector and makes use of a Fourier Transform Infrared Spectrometer for performing the functions of light source and detection (Miller, Weakley, Griffiths, Cauda,

& Bayman, 2017). The discussion below applies to both the photoacoustic method and the NIOSH methods for RCS quantification.

An ideal detector of RCS in the presence of coal and other mineral dust like kaolinite would consist of an absorption measurement with a laser wavelength that is strongly absorbed by RCS and is negligibly absorbed by the other species present. Additionally, the light absorption would occur throughout the entire volume of RCS aerosol so that the absorption measurement would be sensitive to the total mass of SiO_2 per unit volume in the dust sample, as is the current practice used in RCS health measurements.

Figure 3 shows the schematic of a simplified photoacoustic instrument. Sample air enters the instrument on the left, is pulled through the acoustical resonator in the center region and exits on the right. A power modulated quantum cascade laser enters on the left and exits on the right to a laser power meter. The modulation frequency of the QCL is set to match the acoustical resonator frequency. RCS present in the center region will absorb laser light and heat. The heat is then transferred to the surrounding air, resulting in thermal expansion. A micro speaker (not shown) is used to calibrate the acoustical resonator to make sure the proper frequency is maintained. The quantum cascade laser wavelength can be tunable to cover a range of wavelengths for quantifying RCS, kaolinite, and coal dust (Wei, Kulkarni, Ashley, & Zheng, 2017).

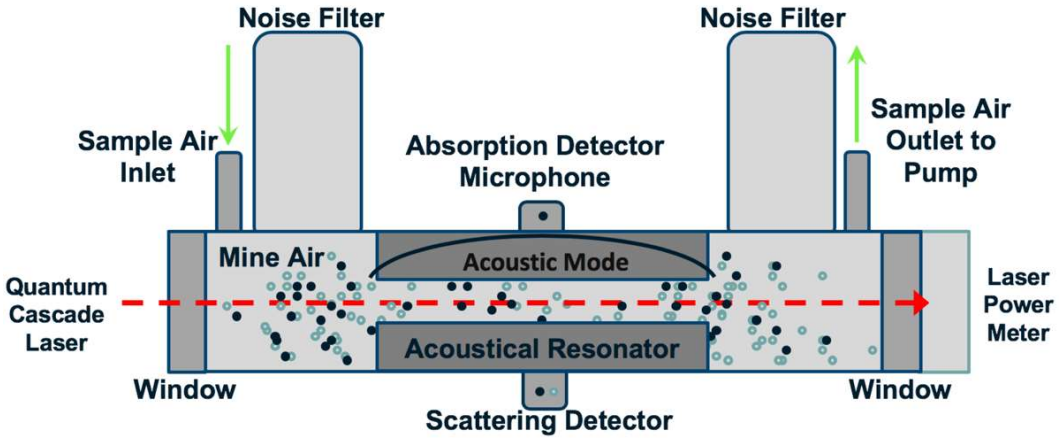

Figure 3: Schematic of the photoacoustic instrument. The half wavelength acoustic resonator is in the center of the instrument. The acoustic mode indicates a pressure antinode at the resonator center and nodes just outside the resonator on each side. The instrument measures both light scattering and absorption. For illustration purposes, aerosol diameter is greatly exaggerated, and concentration is typically much greater than shown in this schematic.

The photoacoustic instrument operation is as follows (Arnott, Moosmuller, Rogers, Jin, & Bruch, 1999). First, the laser light is power modulated with a square wave. Light absorbing aerosols convert the light into heat that is transferred to the surrounding air. Pressure is created in the resonator and a standing wave of sound is produced. The microphone measures the sound at the frequency of the laser power modulation. Finally, the sound signal measures the aerosol light absorption and silica dust mass concentration with a proper choice of laser wavelength that is absorbed by silica. The acoustical resonator is in the center section. The resonance frequency is typically around 1500 Hz as a compromise

between instrument size and thermal response time of the aerosol. 'Acoustic Nodes' are volumes tuned to reflect noise at the operating frequency coming in from the sample inlet and outlet to avoid sound interference to the sensitive microphone within the resonator.

The measurement of silica dust can be achieved by using the photoacoustic equation to relate the sound pressure and laser power to the aerosol light absorption coefficient (Arnott et al., 1999),

$$\boldsymbol{\beta_{abs}} = \frac{\boldsymbol{P_m}}{\boldsymbol{P_L}} \frac{\boldsymbol{A_{res}}}{\boldsymbol{\gamma - 1}} \frac{\boldsymbol{\pi^2 f_0}}{\boldsymbol{Q}} \qquad \text{Equation 1}$$

where P_m and P_L are the microphone pressure and laser power at the resonant frequency f_0 determined with the speaker and microphone; A_{res} is the cross-sectional area of the resonator; γ=1.4 is the ratio of isobaric and isochoric specific heats for air; and Q is the quality factor of the resonator. A calibrated microphone and laser power meter are used so that accurate values are entered in Equation ***1***. The accuracy of this method has been tested by calibration of instruments using light absorbing gases (Arnott, Moosmuller, & Walker, 2000). The aerosol light absorption coefficient is the quantity which is also measured in the filter-based FTIR measurements of RCS (Miller et al., 2017; Wei et al., 2017). Aerosol light absorption at UV, visible, and near IR wavelengths is also used to measure carbonaceous aerosol mass concentrations by photoacoustic and filter-based techniques (Arnott, Hamasha, Moosmuller, Sheridan, & Ogren, 2005). Once the aerosol

light absorption coefficient is measured, the mass concentration of silica dust is obtained in the following manner.

2.3 Theory of Light Absorption by RCS and Kaolinite

2.3.1 Refractive Indices of Alpha Quartz, Kaolinite and Other Minerals

The complex refractive index, *m,* is a material property that determines the interaction of light with matter (K. A. Lewis et al., 2009). The notation used is

$$\boldsymbol{m = n + ik} \qquad \text{Equation 2}$$

where *n* and *k* are the real and imaginary parts. Light absorption is primarily associated with the imaginary part. Figure 4 shows the complex refractive index for many minerals likely to be found suspended in the atmosphere, both as internally mixed combinations and as an externally mixed single composition aerosol. For example, alpha quartz (gray curve) has a relative maxima imaginary part at around 9.2 µm and 12.44 µm due to the resonate interaction of light at these wavelengths with quantum mechanical modes of vibration, and it is larger than other minerals. The most common mineral interferent for RCS determination is kaolinite (Miller et al., 2017), though the spectra in Figure 4 are useful for understanding interference by other minerals. The complex refractive indices of dust are needed to model the infrared radiative impacts of these aerosol (Di Biagio et al., 2014).

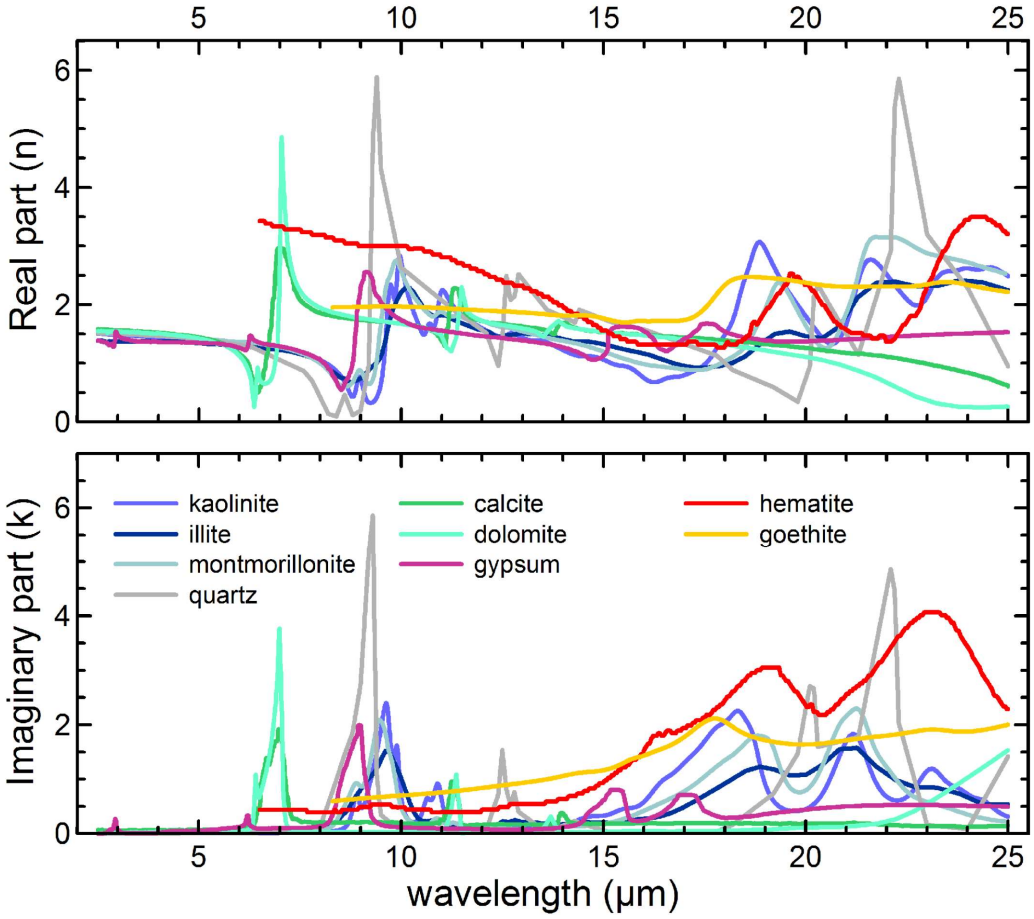

Figure 4: Complex refractive indices for various minerals (Di Biagio et al., 2014).

Alpha quartz has different refractive indices for light with polarization parallel to the 'a' (Figure 5) and 'c' (Figure 6) crystallographic axes. The wavelength range of 8 μm to 13 μm is where the atmosphere is relatively transparent so that aerosol absorption can be measured without much gaseous absorption interference. The complex refractive indices of kaolinite are shown in Figure 7. The real and imaginary parts of the complex refractive index, along with aerosol size and morphology, are used to determine the

amount of light absorption and scattering by these particles. Spherical particles of diameter *D* are assumed. The relationships among aerosol diameter, wavelength of the light source, and complex refractive index will be used to choose a laser wavelength for measuring the mass concentration of SiO_2 dust.

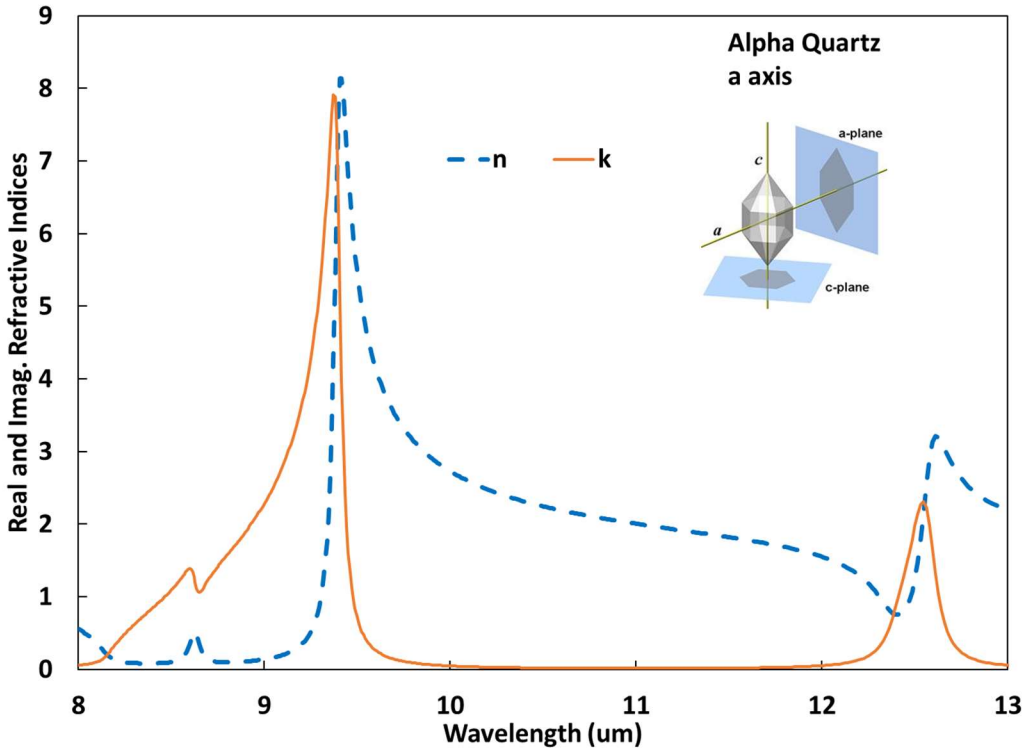

Figure 5: Real and imaginary parts of the refractive indices of alpha quartz for incident light with polarization parallel to the a-axis (Zeidler, Posch, & Mutschke, 2013).

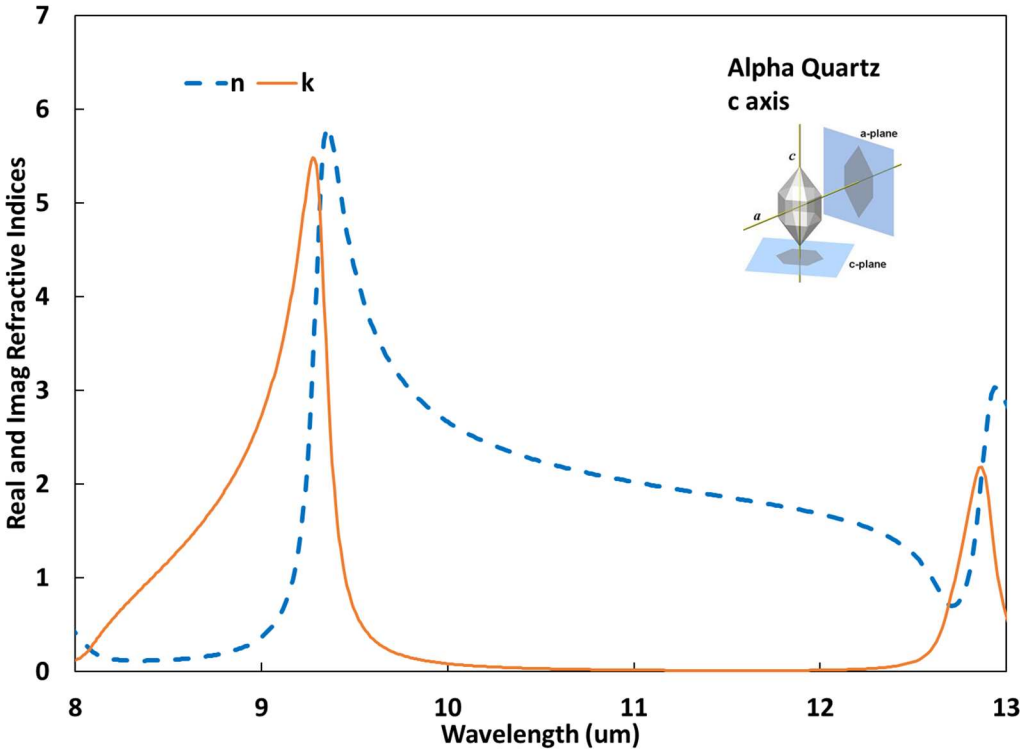

Figure 6:Same as Figure 5 but for the c-axis (Zeidler et al., 2013).

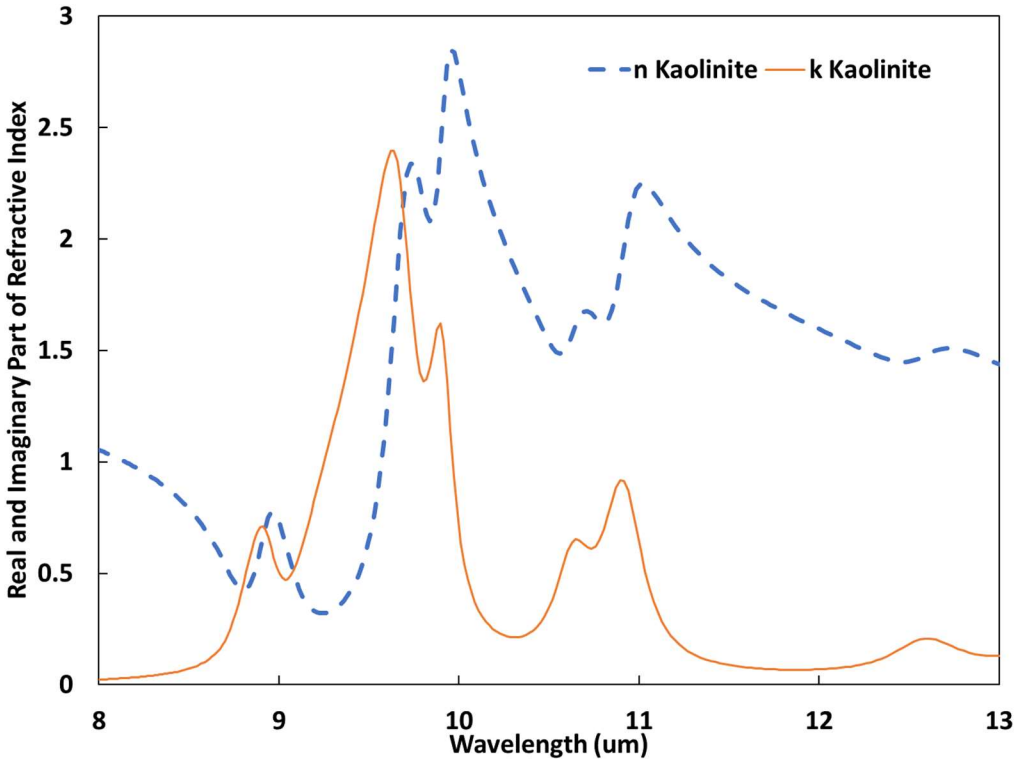

Figure 7:Same as Figure 5 but for kaolinite (Glotch, Rossman, & Aharonson, 2007).

2.3.2 Light Penetration Depth of SiO_2 and Kaolinite Aerosol

The light penetration depth, δ, into an aerosol particle is given by (Moosmuller, Chakrabarty, & Arnott, 2009)

$$\boldsymbol{\delta = \frac{\lambda}{4\pi k}} \qquad \text{Equation 3}$$

where λ is the light wavelength, and k is the imaginary part of the refractive index from Equation 2. This parameter provides a semi-quantitative understanding of the interaction of radiation at various wavelengths with dust aerosol. Figure 8 is a schematic of the light penetration depth of a spherical particle.

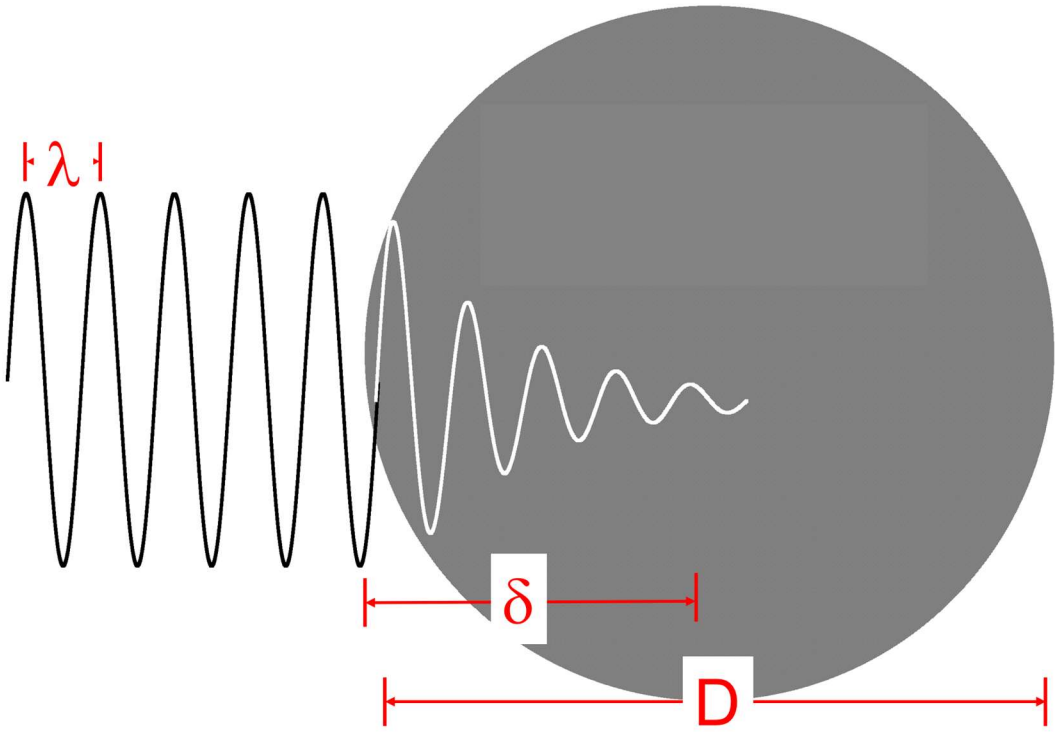

Figure 8:Schematic showing light penetration depth δ into a spherical particle of diameter D.

Three regimes are identified:

- $\delta << D$ Light is absorbed mostly by the surface of the particle, ideal for surface area measurements.
- $\delta \approx D$ Light is absorbed within the aerosol diameter (resonance regime).
- $\delta >> D$ Light is absorbed throughout the entire particle volume, ideal for measuring the mass concentration of the aerosol. However, absorption strength is smaller in this regime.

Large values of the imaginary part of the refractive index result in small light penetration depths. For example, in Figure 6, 9.2 microns corresponds to a peak in the imaginary part of the refractive index. Often, a compromise must be made so that light absorption by the desired species is strong enough to occur over the entire particle volume for mass concentration measurement but is weak for interfering species such as kaolinite (Zeidler et al., 2013). Figure 9 shows the light penetration depth for SiO_2 and kaolinite. The absorption band around 8.5 μm for SiO_2 is associated with a penetration depth less than a micron and is different from that of kaolinite. At 12.8 μm, the light penetration depth for SiO_2 is much greater.

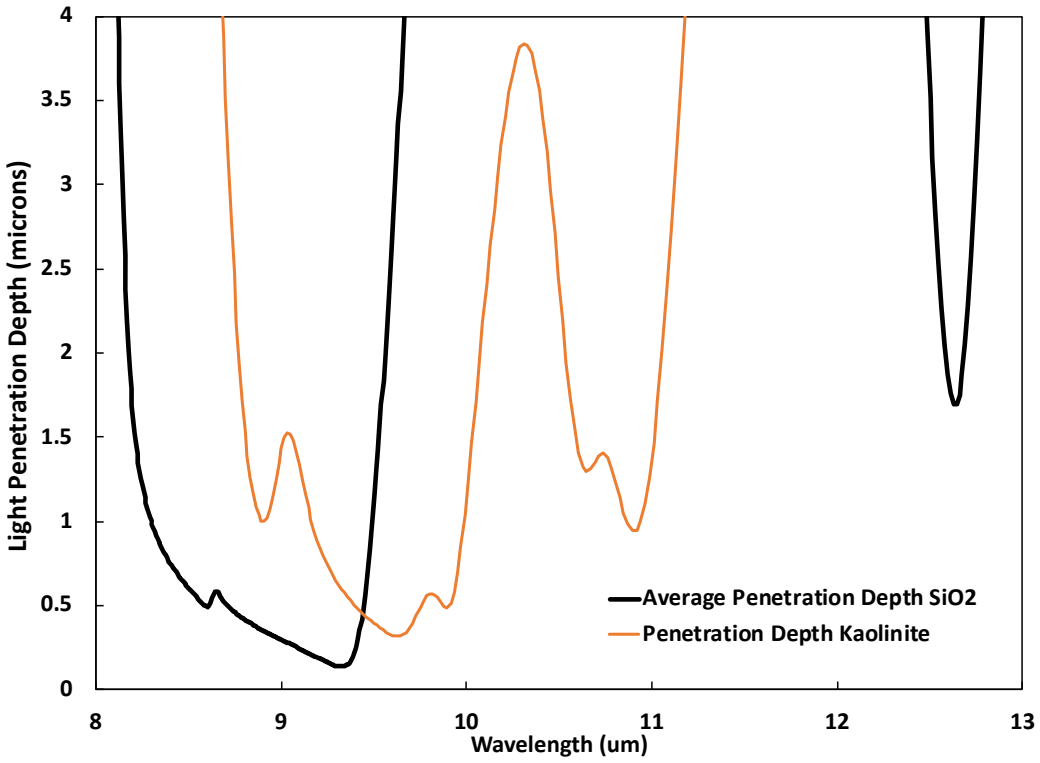

Figure 9:Light penetration depth as a function of wavelength for SiO2 and kaolinite.

2.3.3 Small Particle Limit for Light Absorption by SiO_2 and Kaolinite

The small particle limit for light absorption is based on an analytical solution of the theory for spheres, taking into account only the first term (Moosmuller et al., 2009). It is accurate when the aerosol diameter is much smaller than the light penetration depth. The most useful parameter is the mass absorption efficiency, *MAE*, which is also known as the aerosol absorption cross section per aerosol mass. It is given by:

$$\boldsymbol{MAE = \frac{6\pi}{\rho_p \lambda} IM\left\{\frac{m^2 - 1}{m^2 + 2}\right\}}$$ Equation 4

where ρ_p is the aerosol density (2.65 g cm^{-3} for SiO_2 and 2.6 g cm^{-3} for Kaolinite), m is the complex refractive index of Equation 2, and the IM selects the imaginary part of the quantity in the brackets. Equation 4 depends both on the real and imaginary parts of the refractive index. Especially notice that *MAE* is independent of aerosol diameter; therefore, in this limit, the *MAE,* typically given in units of [m^2/gram], depends only on the total aerosol mass concentration. In this limit, light absorption measurements by photoacoustic instruments and Fourier-Transform Infrared Spectrometers can be expressed as:

$$\boldsymbol{\beta_{abs} = MAE\ \rho}$$ Equation 5

where β_{abs} is the absorption coefficient, and ρ is the desired aerosol mass concentration. The left-hand side of Equation 5 is the quantity measured from Equation 1; the *MAE* may be determined from Equation 4 or from empirical measurements; and thus the aerosol mass concentration is obtained from solving Equation 4 for the desired quantity ρ,

$$\boldsymbol{\rho = \beta_{abs}/MAE}$$ Equation 6

The *MAE* for SiO_2 and kaolinite is shown in Figure 10. The average SiO_2 absorption is obtained from

$$MAE = \frac{1}{3}MAE_{c-axis} + \frac{2}{3}MAE_{a-axis}$$ Equation 7

The factor of 2 in the second term is due to the a-axis being doubly represented as shown in Figure 5. This model assumes that there is no preferred orientation of the SiO_2 crystalline axes relative to the polarization direction of the light.

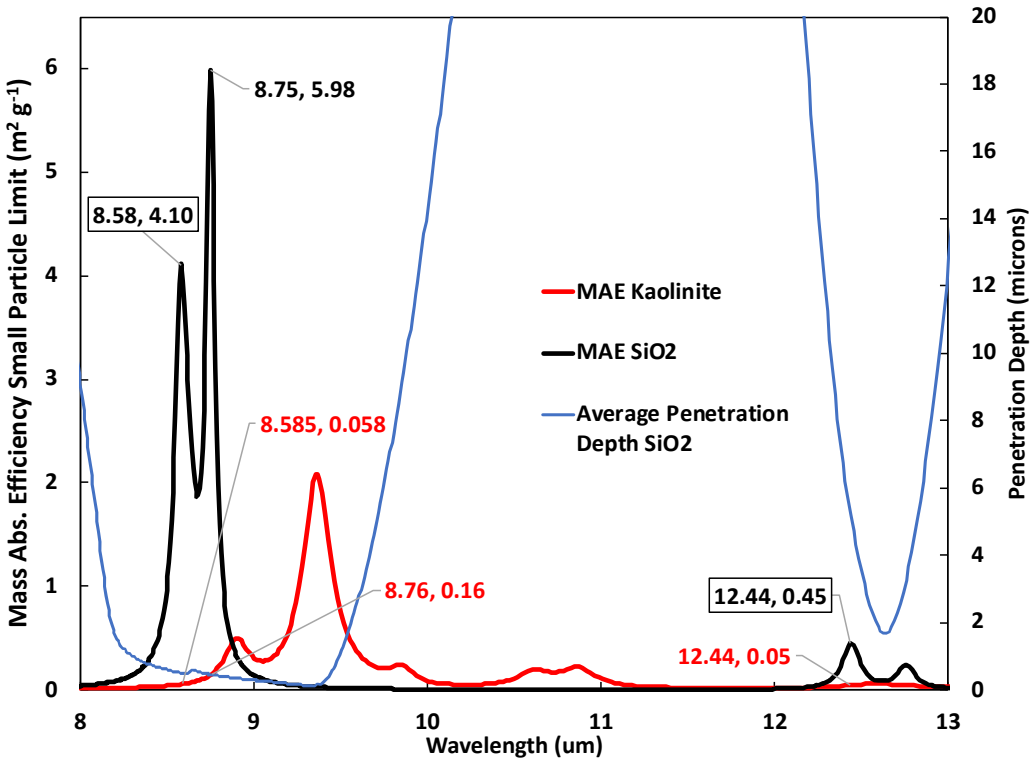

Figure 10: Average MAE for SiO2 and kaolinite (left axis) and the penetration depth (right axis) as a function of light wavelength. Candidate wavelengths for the laser wavelength of the photoacoustic instrument are shown by the numbers printed on the graph.

Figure 10 gives both the MAE and the light penetration depth for SiO_2, along with candidate ordered pairs of values as candidate laser wavelengths. Table 1 summarizes the choices for laser wavelength based on Figure 10. Wavelengths are chosen where the MAE for SiO_2 is large. The best candidate laser wavelengths are shown in bold: $\lambda = 8.58$ μm and $\lambda = 12.44$ μm.

Table 1: Summary of possible wavelengths for the photoacoustic instrument measurement of SiO2 with minimal interference from kaolinite. In comments, green is desirable, and red is not.

λ (μm) (Gerrity, Garrard, & Yeates, 1983)	Wavenumber (cm^{-1})	*MAE* SiO_2	*MAE* Kaolin	δ	Comment
8.58	**1165.5**	**4.10**	**0.058**	**0.5**	**Great kaolinite rejection; small δ**
8.75	1142.9	5.98	0.16	0.459	Okay kaolinite rejection; small δ
12.44	**803.9**	**0.45**	**0.05**	**5.19**	**Larger δ; smaller kaolinite rejection**

2.3.4 Model for the Mass Absorption and Scattering Efficiencies at the Instrument Candidate Wavelengths

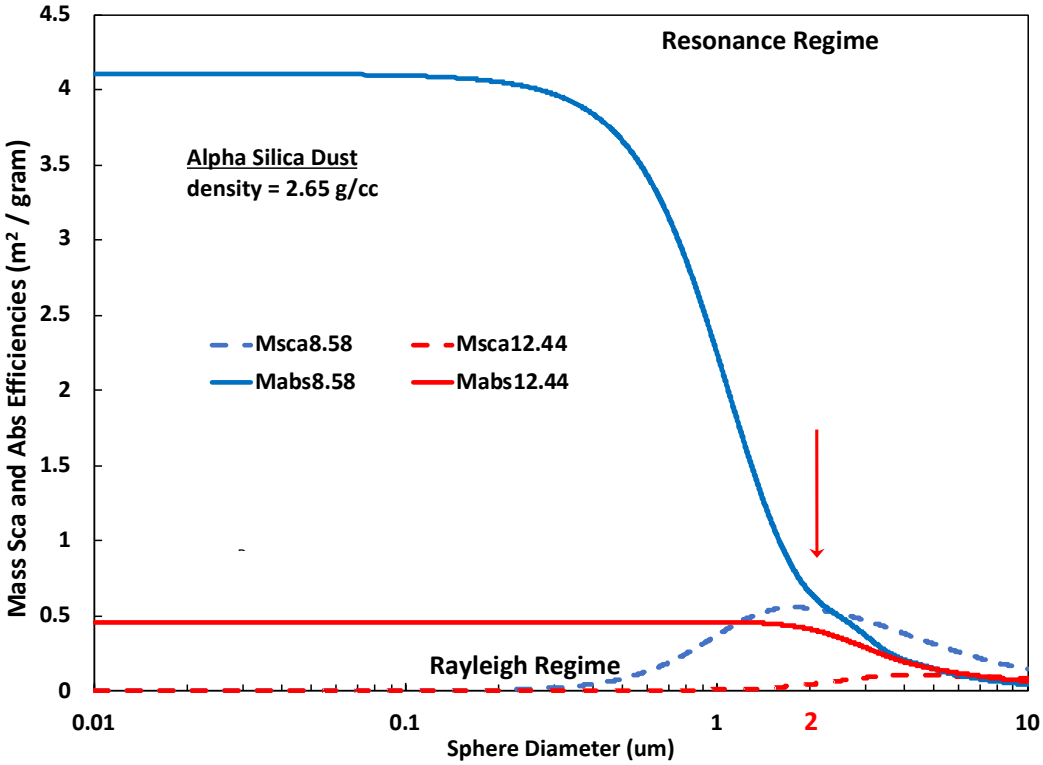

Figure 11: Average SiO2 mass absorption and scattering efficiencies over crystal axes orientation calculated from Mie theory as a function of aerosol diameter for 8.58 and 12.44 microns.

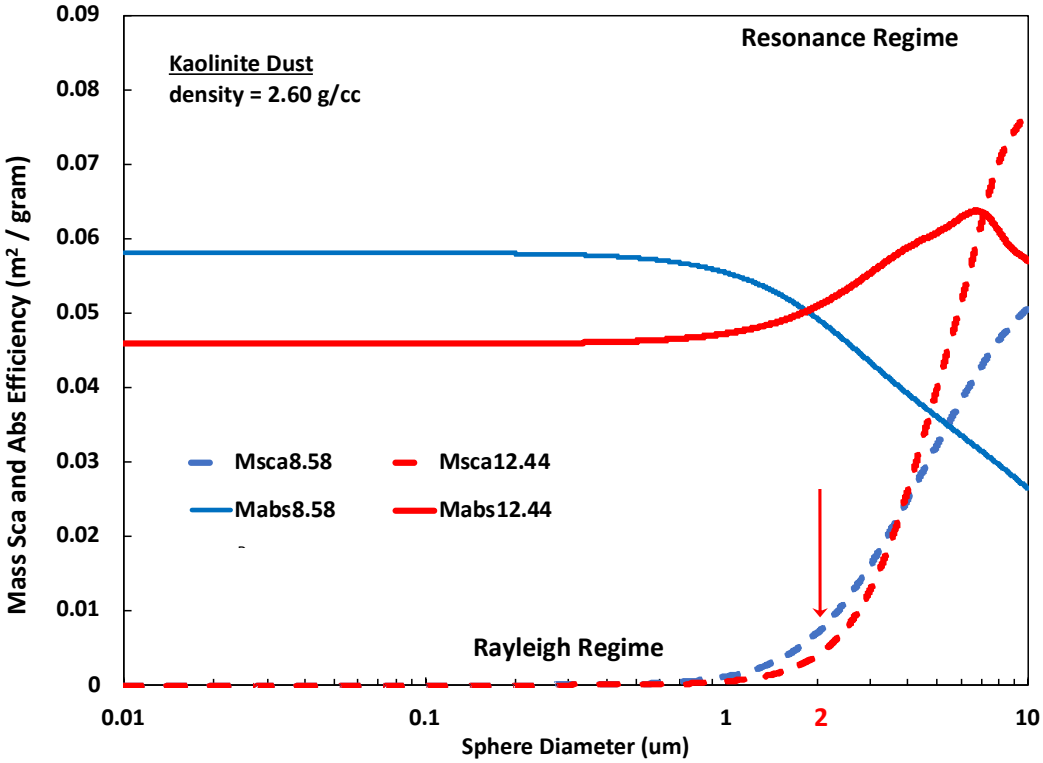

Figure 12: Same as Figure 11, but for kaolinite.

Figure 11 and Figure 12 show the Mie theory (Moosmuller et al., 2009) calculated mass scattering and absorption efficiencies for SiO_2 and kaolinite, respectively, at the candidate wavelengths. The flat portions of the MAE curves for SiO_2 are associated with the wavelength range where light absorption is independent of aerosol diameter, ideal for determination of the aerosol mass concentration. Figure 11 shows that the flatness of the mass absorption efficiency curve for a wavelength of 12.44 μm extends to an aerosol diameter of around 2 μm, whereas at 8.58 μm, it extends only to about 1 μm before steeply declining. The mass absorption efficiency for kaolinite is much smaller in

comparison to SiO_2 at these wavelengths, as shown in Figure 12. Thus, the ideal laser wavelength is theoretically 12.44 μm because it is a tradeoff between moderate-to-strong absorption and penetration of the laser radiation into the particle.

2.4 Mass Absorption Efficiency for Coal, Water Vapor, and Carbon Dioxide Compared to SiO_2 and Kaolinite

Research has been done previously on the real and imaginary refractive indices for coal (Foster & Howarth, 1968). These data were digitized and used for computations of the optical properties of coal. Assuming a coal mass density of 1.4 g cm^{-3}, the small particle limit mass absorption efficiency for bituminous coal was computed and is shown in Figure 13, along with those of SiO_2 and kaolinite. In reported previous research, coal dust was not a strong interferent for the FTIR measurements of SiO_2 (Miller et al., 2017). The mass absorption efficiency of water vapor is apparent in Figure 13 as well. Theoretical absorption spectra were computed using spectralcalc.com. Notice that there are several peaks in H_2O's mass absorption efficiency located right around the peaks related to SiO_2. These peaks represent strong interference by H_2O vapor. Special care must be taken to choose a wavelength for SiO_2 quantification that does not include one of these peaks. However, the presence of these peaks has an advantage. It has been previously shown that light absorbing gases can be used to calibrate photoacoustic instruments (K. Lewis et al., 2008). If the photoacoustic instrument has a relative humidity and air temperature sensor built into it, it can quantify the water vapor concentration. With this value known,

a wavelength can be chosen to measure the absorption coefficient, β_{abs}, of water vapor. Because this allows for correlation between the water vapor's measured absorption coefficient and calculated concentration, this information can be used to calibrate the photoacoustic instrument's SiO_2 concentration calculation.

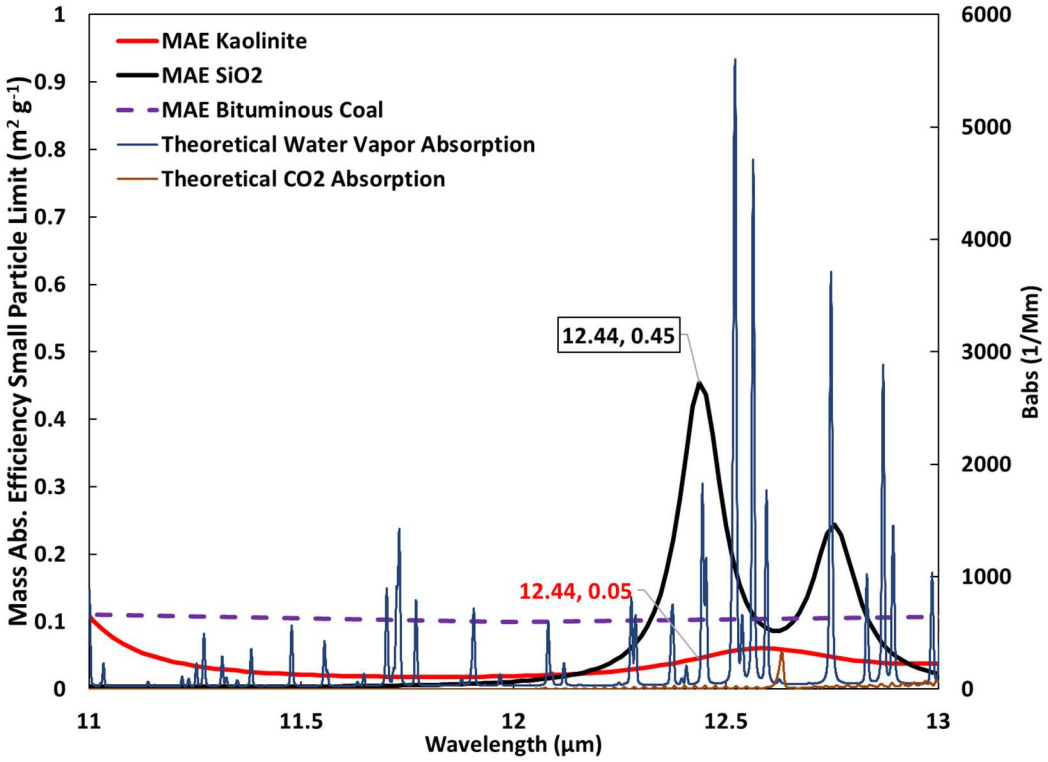

Figure 13: Small particle limit of the mass absorption efficiency for SiO2(black curve), kaolinite (red curve), and bituminous coal. Also includes absorption coefficient for water vapor and carbon dioxide.

2.5 Effect of Acoustic Resonant Frequency and Photoacoustic Response

The choice of acoustic resonator frequency is related to resonator geometry and size. It is important for quantitative measurements of light absorption. This is because laser heated aerosols have a finite time for that heat to transfer to the surrounding air between laser pulses (Moosmuller et al., 2009). The response time τ for heat to diffuse from an aerosol of radius r to the surrounding air having thermal conductivity κ_{air} is:

$$\boldsymbol{\tau = \frac{r^2\, \rho_{RCS}\, c_{RCS}}{3\kappa_{air}}} \qquad \text{Equation 8}$$

where ρ_{RCS} and c_{RCS} are the density and heat capacity per unit mass of RCS. The response of the photoacoustic signal at a frequency f as affected by heat transfer time is:

$$\boldsymbol{\alpha = \frac{1}{1 - i\, 2\pi f \tau}} \qquad \text{Equation 9}$$

where i is the unit imaginary number. Figure 14 shows the amplitude and phase response of laser heated RCS aerosol as a function of aerosol diameter. The left y-axis shows the relative amplitude of the aerosol light absorption signal and ideally would have a value of unity for all aerosol diameters. 500 Hz operation is closer to ideal than is 1500 Hz.

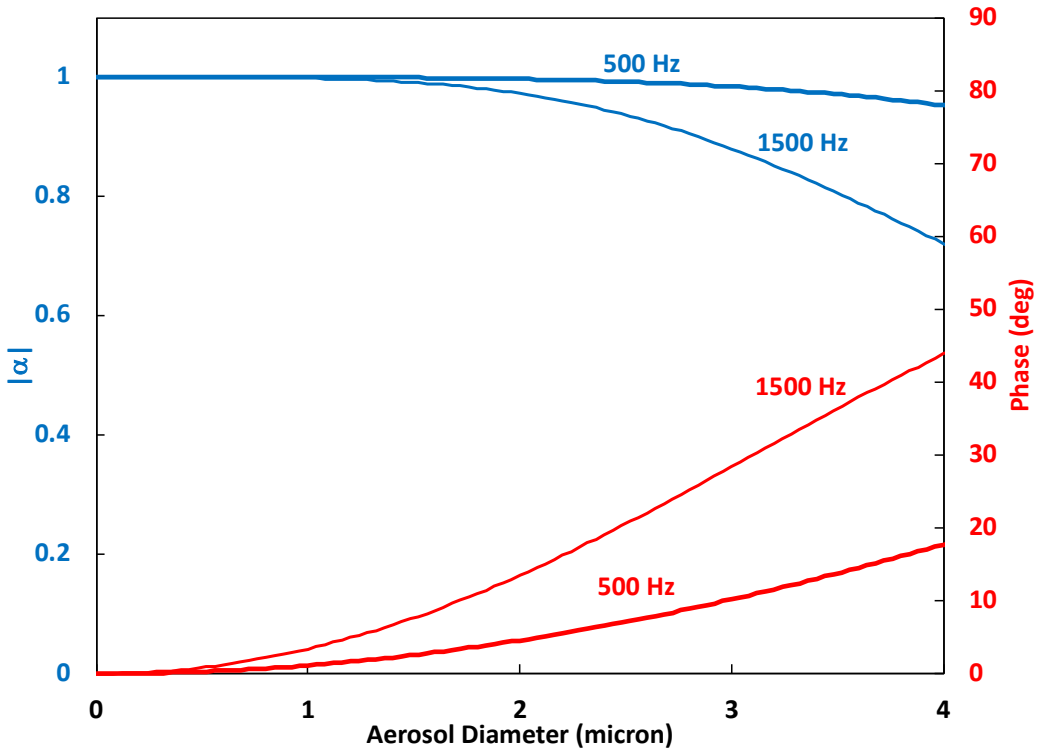

Figure 14: Amplitude (left y axis) and phase (right y axis) of the modeled photoacoustic signal response for RCS as a function of aerosol diameter at two acoustical frequencies. 500 Hz operation has a flatter (and thus better) amplitude and phase response because heat can come out of the aerosol during laser beam modulation at the lower frequency.

Recent research has demonstrated the utility of a miniature Helmholtz resonator-based photoacoustic instrument for methane detection using a quantum cascade laser at 3.36 microns wavelength (Rouxel et al., 2016). The instrument used was approximately 3" long, though operated at 2,000 Hz, which is rather high for silica detection because of the higher response time. However, their research establishes the utility of Helmholtz resonator detectors so that a compact 500 Hz device may be developed for RCS detection.

A lower frequency instrument is desirable for dust measurements in order to mitigate phase-lag. Additionally, aerosol detection is more challenging than trace gas detection because special precautions must be employed to manage the eventual dirtying of the resonator windows by aerosol deposition.

2.6 Approaching a Photoacoustic RCS Measurement System

Figure 13 suggests that RCS has a strong absorption feature at 12.44 microns, with possibly some interference by kaolinite and coal dust to be expected. Kaolinite has relatively strong absorption at 11 μm with some coal dust interference, though small RCS interference. Coal dust is the dominant absorber at 12 μm. A tunable quantum cascade laser photoacoustic instrument operating in this spectral range can thus be used to determine the concentration of RCS and correct for interference by coal and kaolinite dust. Absorption by water vapor can be used to check the instrument calibration. Carbon dioxide gas does not interfere with measurements in this range. Additionally, it is desired to have a photoacoustic instrument operating at a frequency of around 500 Hz so that aerosol thermal response time does not introduce aerosol size dependent response to the instrument, as shown in Figure 14.

Chapter 3: Methods

3.1 Photoacoustic Instrument Design

The prototype of the tunable quantum cascade laser photoacoustic instrument was adapted from an existing photoacoustic instrument originally used for measuring ambient black carbon concentrations. This adaptation was accomplished in 4 steps. The first step was to replace the currently attached laser with the tunable quantum cascade laser. The laser acquired for this was a Daylight Solutions Hedgehog, model number 31100-HHG. Gold-plated alignment mirrors are used for fine alignment adjustments along the laser's beam path within the photoacoustic resonator. This laser has a power of less than 205 milliwatts, a max pulse duration of 1 microsecond, and a wavelength range of 10.93 μm to 13.79 μm. During experiments, our scans always took place between 11 μm and 13 μm, as the laser's power curve revealed that the power output from the laser, when operated outside of these bounds, was too low, which increased the signal noise. The maximum modulated power at the resonance frequency of the photoacoustic cell was only around 8 mW. The laser is modulated at 5 MHz with a duty cycle of 10%, and again modulated at around 1500 Hz with a duty cycle of 50% to drive aerosol light absorption in the photoacoustic instrument. The ability to measure low concentrations of RCS depends on having high modulated laser power.

Next, the laser windows into the resonation chamber had to be replaced with windows that have high transmission at the operating wavelengths. Potassium bromide, a common salt used for infrared optics, was the material chosen for the laser windows due to the material's high transmissivity in mid-to-far infrared wavelengths, as shown in Figure 15.

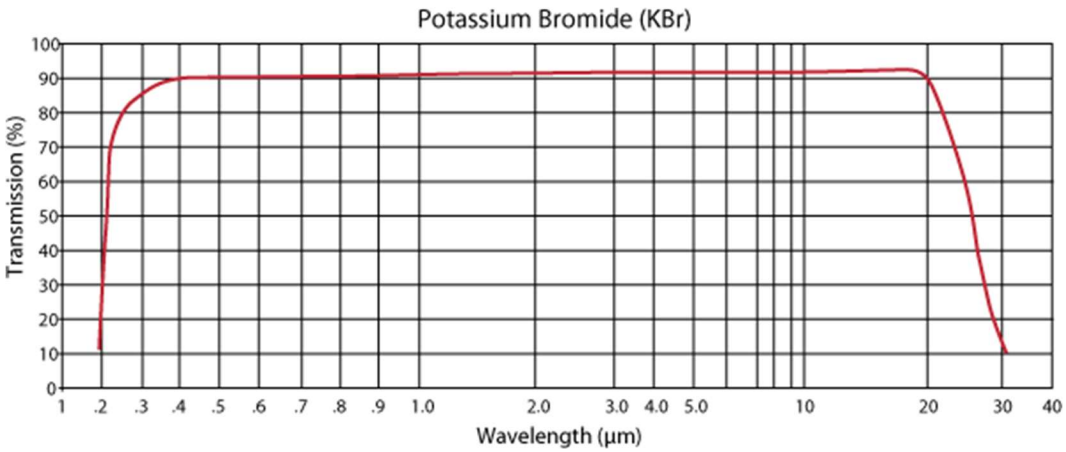

Figure 15: Transmission percentage of potassium bromide with wavelength. (Edmund Optics)

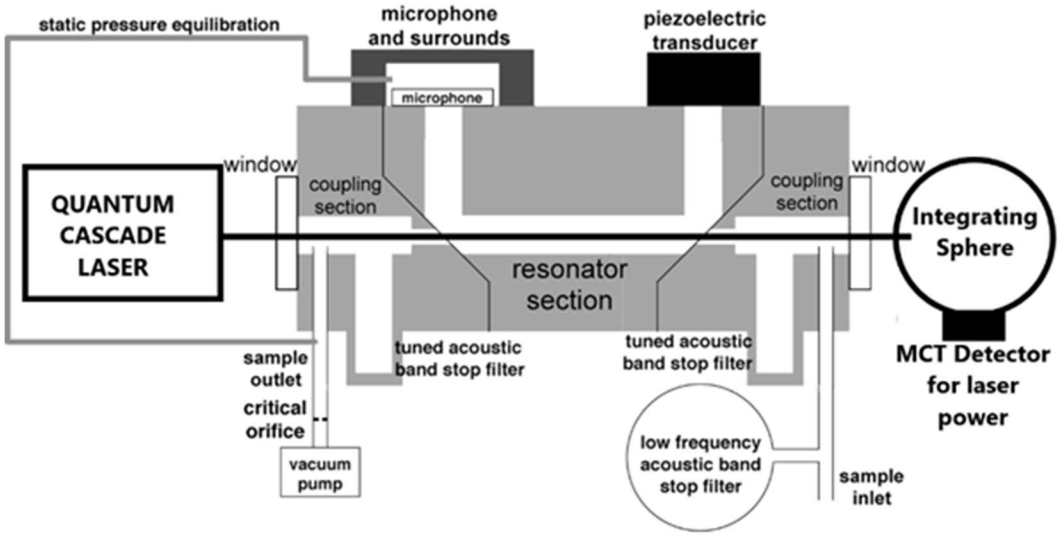

Figure 16: Diagram of the photoacoustic instrument.

In Figure 16, sample air is pulled through the resonator section with a vacuum pump, while the QCL is power modulated. The laser beam enters the window on the left, interacts with the aerosol in the resonator section, and then exits on the right. The laser light that is not absorbed or scattered then enters the integrating sphere, where a mercury-cadmium-telluride (MCT) detector records the laser power. The modulation frequency of the QCL is set to the frequency of the resonator, which in this case is around 1500 Hz. The photoacoustic instrument has the capability of modifying this frequency depending on the air temperature within the resonator. The energy of a photon generated by the QCL is transferred to the aerosol particle upon absorption, which is then transferred again to the air surrounding the particle, causing thermal expansion. The modulation of the light source thus creates a sound wave as the air expands and

contracts, which is measured by the microphone using phase-sensitive detection (Arnott et al., 2005). In order to quantify airborne respirable silica, kaolinite, and coal, the QCL is tunable and covers the range of 11 μm to 13 μm (Wei et al., 2017). By using sound pressure P_m, laser power P_L, resonator cross sectional area A_{res}, ratio of specific heats γ for air, resonator quality factor Q, and resonance frequency f_0, the aerosol light absorption coefficient is given by Equation 1 (Arnott et al., 1999). When combined with an empirical or theoretical mass absorption efficiency (see Figure 13), silica mass concentration is obtained from Equation 6.

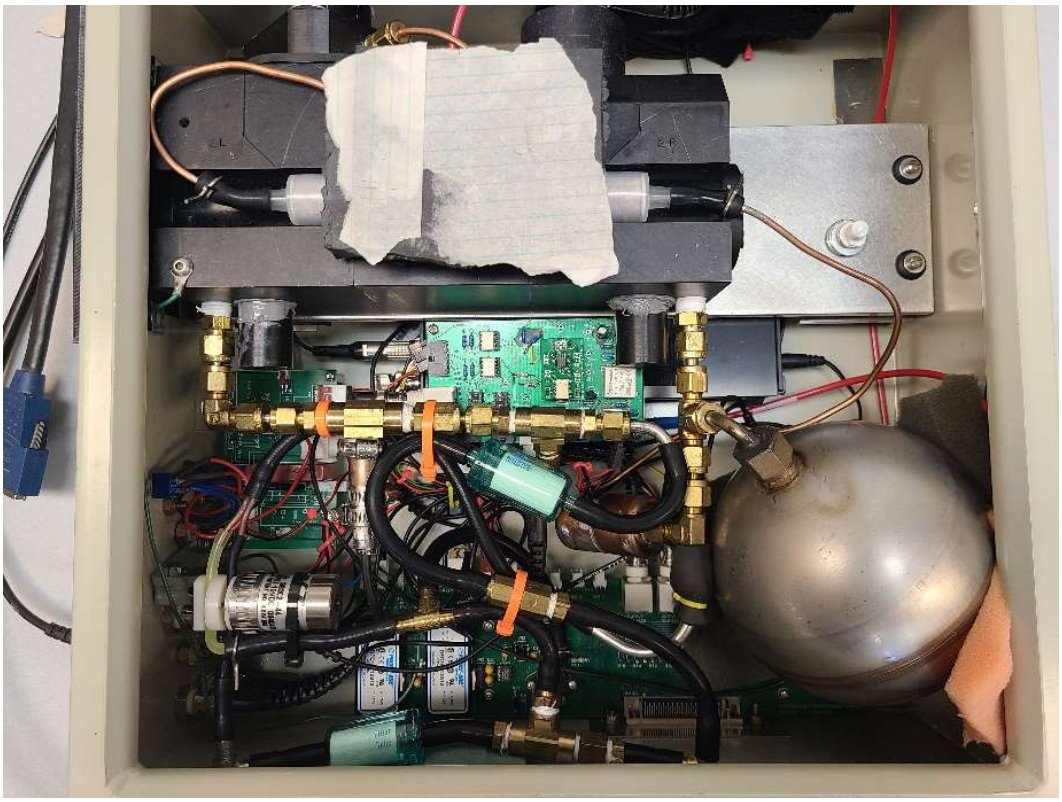

Figure 17: An interior view of the prototype photoacoustic instrument.

Figure 17 shows the innerworkings of the prototype QCL photoacoustic instrument. The resonation chamber is the black box at the top left of the instrument. This is where the sensitive microphone measures the sound generated by the oscillating laser interacting with the sampled aerosol. The laser from the QCL enters the chamber from the left via a potassium bromide window attached to the chamber. After passing through the chamber, the laser light exits on the right, through another potassium bromide window, where it is collected by the integrating sphere and measured by the MCT detector.

Figure 17 also shows much of the internal aerosol piping used by the instrument to transport sampled air to and from the resonation chamber. Helmholtz resonators attached in series to the resonation chamber are used as dampers to decrease noise induced by the pump and the inlet system, allowing for a cleaner microphone signal. Two translucent, blue cylinders housing white air filters can also be seen connected to the aerosol piping via rubber tubing. The air filters are used to calibrate and zero the instrument periodically by switching air flow through the filters and allowing clean, filtered air to be measured by the instrument. This process, along with all general functions of the instrument, are controlled by a LabView program running on a connected

computer. Additionally, there is a relative humidity sensor that resides within the flow of the instrument.

The integrating sphere and MCT detector are shown in Figure 18. The integrating sphere's purpose is to intercept the laser after it exits the resonation chamber and dilute it so that the beam cannot damage the photodetector by focusing directly onto the detector. In this case, the MCT detector used for this purpose was taken from a defunct FTIR. The device is contained within a small dewar that holds liquid nitrogen. The detector

must be cooled by liquid nitrogen when in use because of its sensitivity to infrared radiation and to reduce the effects of thermal noise created in the detector.

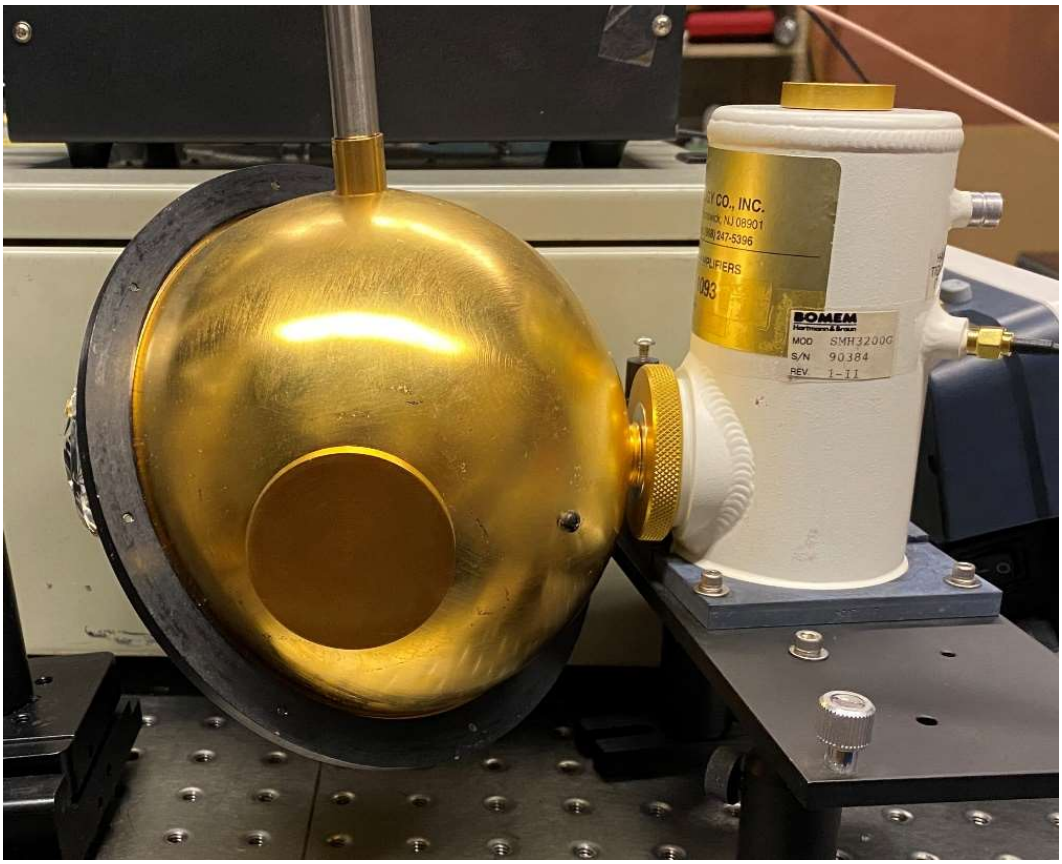

Figure 18: Integrating sphere with MCT detector.

Due to the signal strength from the MCT detector, the instrument design also needed to include an operational amplifier (op amp) as part of the signal circuit. The signal from the photodetector is fed into an op amp circuit to strengthen the signal. The signal from the op amp circuit is then used by the photoacoustic instrument as a measurement of laser power output. The op amp schematic in Figure 19 is the current configuration for

the photoacoustic instrument. The resistance of the MCT detector is about 80 ohms when not being illuminated. The resistance decreases as the detector receives infrared radiation. This, coupled with the 220-ohm resistor connected to the 5-volt supply, creates a voltage divider, while a 0.1 microfarad capacitor and the 200 kOhm resistor make up a high-pass filter. In this case, the op amp is acting as a noninverting amplifier.

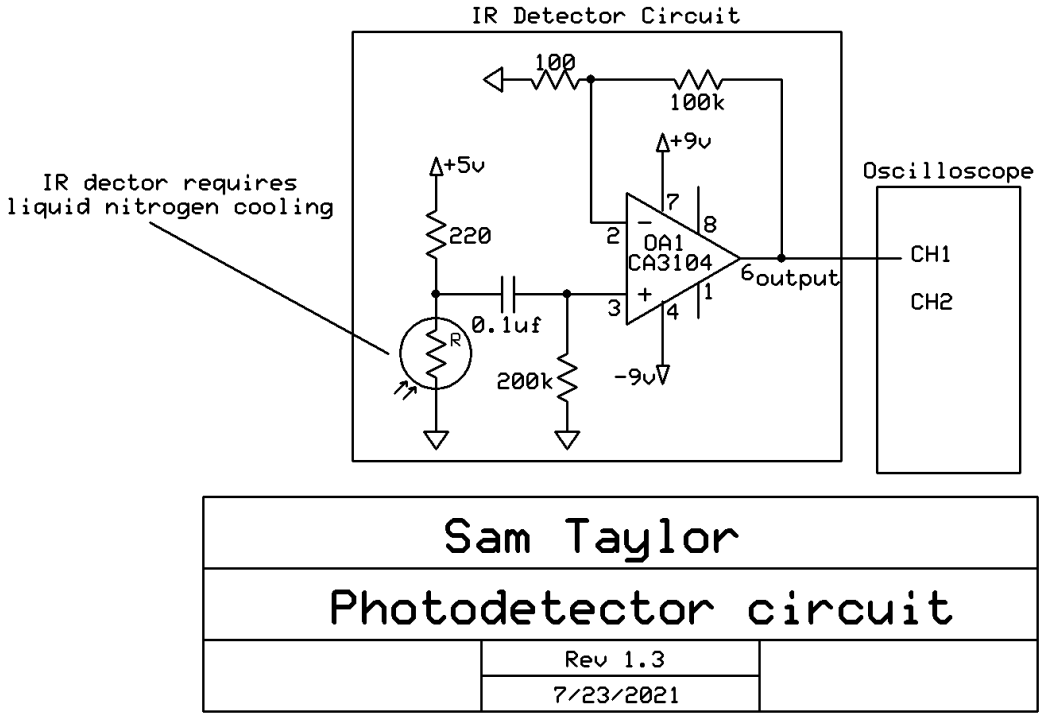

Figure 19: Operational amplifier circuit for the MCT photodetector.

3.2 Aerosol Testing Chamber

Figure 20: Aerosol chamber in UNR's ventilation lab.

Due to the hazardous nature of RCS, coal dust, and particles of respirable size in general, experiments with airborne dust must be safely contained within an airtight chamber that can be quickly ventilated. NIOSH has developed its own such aerosol chamber for testing instruments safely. This chamber is known as Marple Chamber (Marple & Rubow, 1983). The aerosol chamber within UNR's ventilation lab is similar in nature but smaller than Marple Chamber. Figure 20 shows the UNR aerosol chamber, where all dust experiments involved with this project to date have taken place. The black

chamber (right) is a sealed structure of 1.7x0.8x2 meters and an internal volume of 2.7 cubic meters (Nascimento et al., 2021). Feedthrough fittings have been fastened to the front of the chamber to allow for sampling directly from the chamber after the aerosol is suspended within it. A large blower is also attached via sealed PVC pipes into the chamber to allow for quick and easy ventilation of the chamber at the end of experiments. In order to disperse dust within the chamber, a metal mortar is used to hold the dust, and an air hose connected to a compressed air source was fixed above it. Once the chamber is sealed, the compressed air can be fired into the mortar to safely disperse the dust within the chamber. Other precautions to prevent exposure were taken, including the use of a TSI DustTrak to monitor PM concentrations outside of the chamber and N95 dust masks and respirators for anyone in the room during the experiments.

3.3 NIOSH End-of-Shift FTIR Method

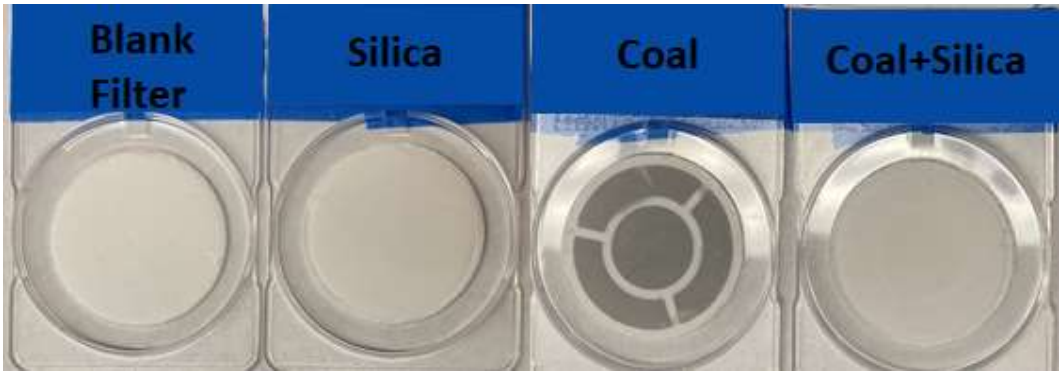

Figure 21: Examples of filter samples taken during testing (Nascimento et al., 2021).

The NIOSH end-of-shift method for monitoring silica is a filter-based aerosol monitoring technique. As discussed in earlier, it was developed as a way to improve silica

concentration reporting times for mine sites (Pampena et al., 2020). The following description details the use of this technique throughout the study. The method requires a number of materials and instruments in order to utilize it. First, a cyclone with a d50 cut point of 4 μm when used at 2.5 liters per minute is necessary to ensure that only the respirable component of the aerosol is measured. In this case, an "SKC-type" Zefon International ZA0060 aluminum cyclone was used. In line with the cyclone is a filter cassette containing a 37 mm PVC aerosol filter, which will collect the PM_4 aerosol. The filters used were Zefon International REF FSP37R PVC filters. Zefon International REF 745PVC-CF-FTIR cassettes were used to hold the filters. Finally, an air pump that is operating at 2.5 liters per minute is used to pull air through the cyclone, cassette, and filter. The sampling apparatus is operated for a short period time while the aerosol is present within the chamber.

Once a filter sample is obtained, the filter is labeled and stored appropriately until it can be analyzed within a Fourier-transform infrared spectrometer (FTIR), as directed by the NIOSH method. The FTIR spectrometer used for this study is a Thermo Fisher Scientific NICOLET 380 FT-IR. Other FTIR models from different brands are usable for this method, so long as they are able to do transmission measurements of a sample filter over a spectral range of 4000 cm^{-1} to 400 cm^{-1} with a resolution 4 cm^{-1} (NIOSH, 2020; Pampena et al., 2020). The NIOSH method recommends using a blank, unused filter as a background standard for the FTIR transmission (Pampena et al., 2020). In this case, a blank filter

selected from the same batch as the one used for sampling should be used in the FTIR during the background recording phase of the measurement. This is done to eliminate the filter media's influence on the transmission spectra so that only the transmission spectrum of the sampled dust is reported. While this is effective, an additional step was taken during this study to further minimize the influence of the filter's media on the data. By collecting a reference transmission spectrum of the sample filter before it is used for sampling, the filter's effect on the dust spectrum can be nearly eliminated by dividing the sampled filter's spectrum by its reference spectrum. This proved to the be most effective method for obtaining accurate spectra of silica dust and was the primary method use to normalize the spectra throughout this study.

After a transmission spectrum for a sampled filter is obtained, the average silica concentration over the sample period can be calculated from the collected data. To accomplish this task, NIOSH's proprietary software, the Field Analysis of Silica Tool, is used. In some circumstances, FAST can do these calculations from the transmission spectra alone. For this project, the parameters were manually calculated. Firstly, the transmission spectrum must be converted into an absorbance spectrum. This conversion is given by

$$\boldsymbol{Absorbance} = -\boldsymbol{log}\mathbf{10}\left(\frac{\boldsymbol{Normalized\ Transmission}}{\mathbf{100}}\right) \qquad \text{Equation 10}$$

where *Normalized Transmission* denotes the sample transmission spectrum after it has had the filter media's transmission divided out. Because the strongest absorbance for silica falls on the spectral range of 815 cm^{-1} to 770 cm^{-1}, the FAST software requires the value of the area beneath the absorbance curve in this spectral range to calculate a silica concentration. The concentration obtained from this method is the average silica concentration over the time period of sampling. It should be noted that this is only a concentration for silica. If the filter was sampled during an experiment that contained other mineral dusts, it will not include these in the concentration. However, because kaolinite is considered an interferant when measuring silica concentrations in this way, the FAST software has the ability to account for this. The correction is made by calculating the area under the absorbance spectrum over the spectral range of 930 cm^{-1} to 900 cm^{-1} and inputting the result into FAST in the correct field. Currently, this is the only interferant for which the FAST software has a correction.

For this project, the silica concentrations obtained via this method are used as the standard for comparison for the SPS30 and APS reported PM_4 concentrations, and for the photoacoustic silica concentrations calculated from the absorbance coefficient.

3.4 SPS30 Description

The Sensirion SPS30 is a small, low-cost air quality sensor that utilizes aerosol optical properties to count aerosol particles (Sensirion, 2020). This instrument consists of a 660 nm laser with the focal point just above a photodiode. When a particle crosses the beam path of the laser, the scattered light will contact the photodiode, allowing the instrument to count the particle. The strength of the scattering determines how the instrument will size the particle. The SPS30 has two vents: an intake vent and outflow vent. The outflow vent has a fan attached that pulls sampled air in the intake vent and through the instrument's aerosol channel before it leaves via the outflow vent.

In order to further test the results of data collected from the photoacoustic instrument and the NIOSH end-of-shift method described in section 3.3, the SPS30 was chosen to monitor PM concentrations within the aerosol chamber. Because the NIOSH method reports only silica concentrations, the SPS30 can be used as a comparison in certain situations. When only silica dust is used within the chamber, the SPS30 and NIOSH method should report similar PM concentrations. When mixes of mineral dusts containing silica are measured, then the PM concentrations reported by the SPS30 should be proportionally higher than the NIOSH method, contingent upon the amounts and types of dusts mixed. However, if a mineral dust not containing SiO_2 were used, the SPS30 could not be compared to the NIOSH method, as the NIOSH method cannot currently report concentrations for any dust type other than silica. The SPS30 will still report concentrations in this case, but without a useful comparison to the NIOSH method.

3.5 APS Description

The TSI Aerodynamic Particle Sizer (APS) is a research-grade aerosol monitoring instrument that is capable of counting and sizing particles (TSI, 2013). Sampled air is pulled into the instrument via an inlet located on the top of the instrument. The instrument requires a flow rate of 5 liters per minute to operate. The flow is divided, with a 1 liter per minute flow rate inside of the sample flow and a 4 liter per minute sheath flow. The sample flow is funneled through a nozzle, where it rejoins the filtered sheath flow. By utilizing a sheath flow with the sampled air, the flow rate can be increased while simultaneously forcing the aerosol to the center of the flow, setting the stage for the next step. The sampled air is then passed through an orifice into the optics chamber, which has the effect of accelerating particles within the center of the flow. This causes the smaller particles to reach a higher velocity than the larger particles as they pass through the optics chamber. A split beam in the optics chamber acts as the measurement method. The instrument calculates the time of flight by detecting light scattered from the particle as it crosses the beam paths in sequence. An elliptical mirror beneath the detection zone allows for more efficient collection of light scattered by particles (TSI, 2013). The mirror focuses the scattered light onto an avalanche photodiode, which acts as the particle detector. Once measurement is completed, the sampled air is drawn through a filter and then exits the instrument. Figure 22 visualizes this process.

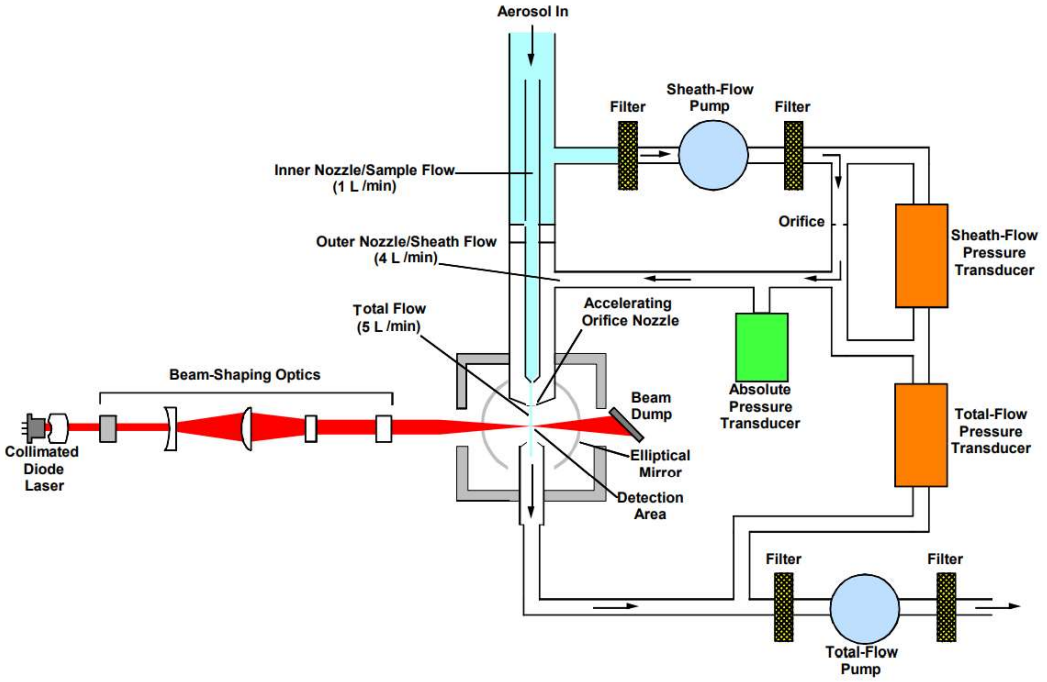

Figure 22: APS Instrument Theory of Operation

For this project, the APS was used as an additional means of monitoring PM concentrations within the aerosol chamber for comparison to the photoacoustic instrument, the SPS30, and the NIOSH FTIR technique. It was also used to collect size distributions during sampling.

Chapter 4: Results

4.1 Water Vapor Absorption Coefficient Spectra

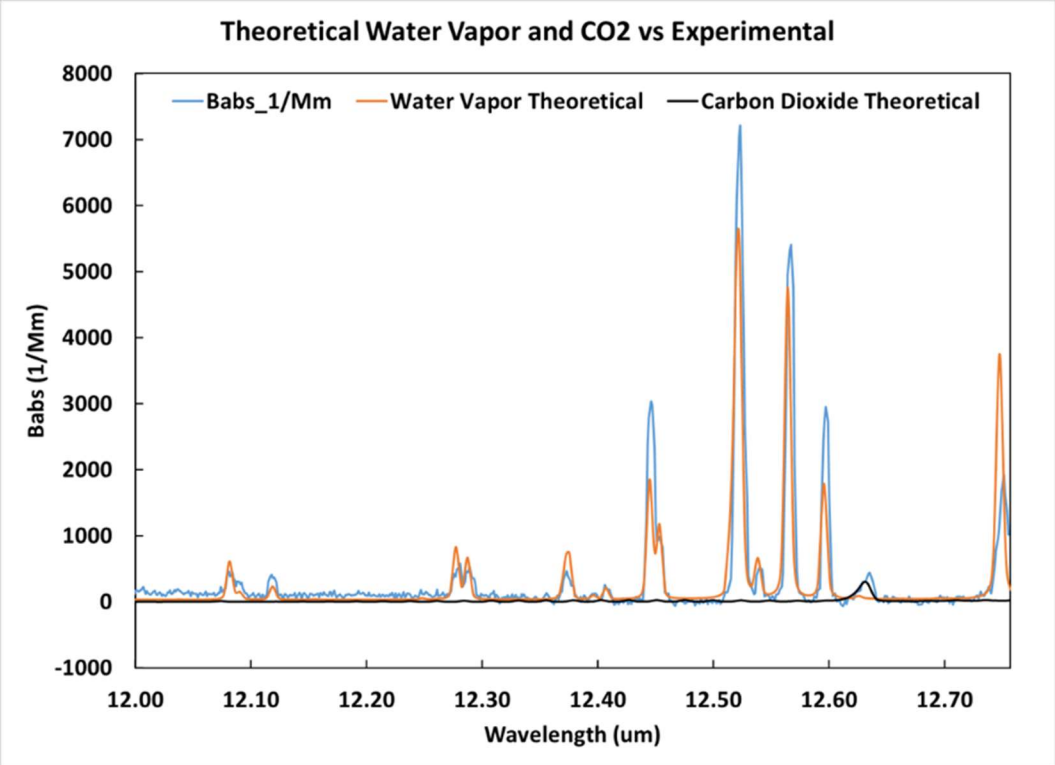

Figure 23: Theoretical and Measured Water Vapor Absorption Coefficient Spectra

Because the photoacoustic instrument will be operating in the mid-infrared, one of the big concerns could be interference by water vapor and carbon dioxide absorption. For this reason, it is important to understand where the most prominent absorption peaks by these gases exist within the spectral region of interest. Figure 23 shows the theoretical and measured absorption coefficient spectra for water vapor and carbon dioxide. Because of the extremely strong absorption by water vapor near to where silica should be absorbing (12.2 μm to 13 μm), this could pose a problem. For this reason, it will be

important to choose a monitoring wavelength that falls distinctly between the water vapor absorption peaks. However, the presence of the water vapor lines in the spectra is not a bad thing either. As in discussed in section 2.4, by using a relative humidity sensor within the flow of the instrument, the water vapor concentration can be calculated and used to calibrate the instrument (K. Lewis et al., 2008). Carbon dioxide poses less of a problem, and its interference is easily avoided since it does not overlap with silica's strongest absorption wavelengths.

4.2 Silica Absorption Coefficient Spectra

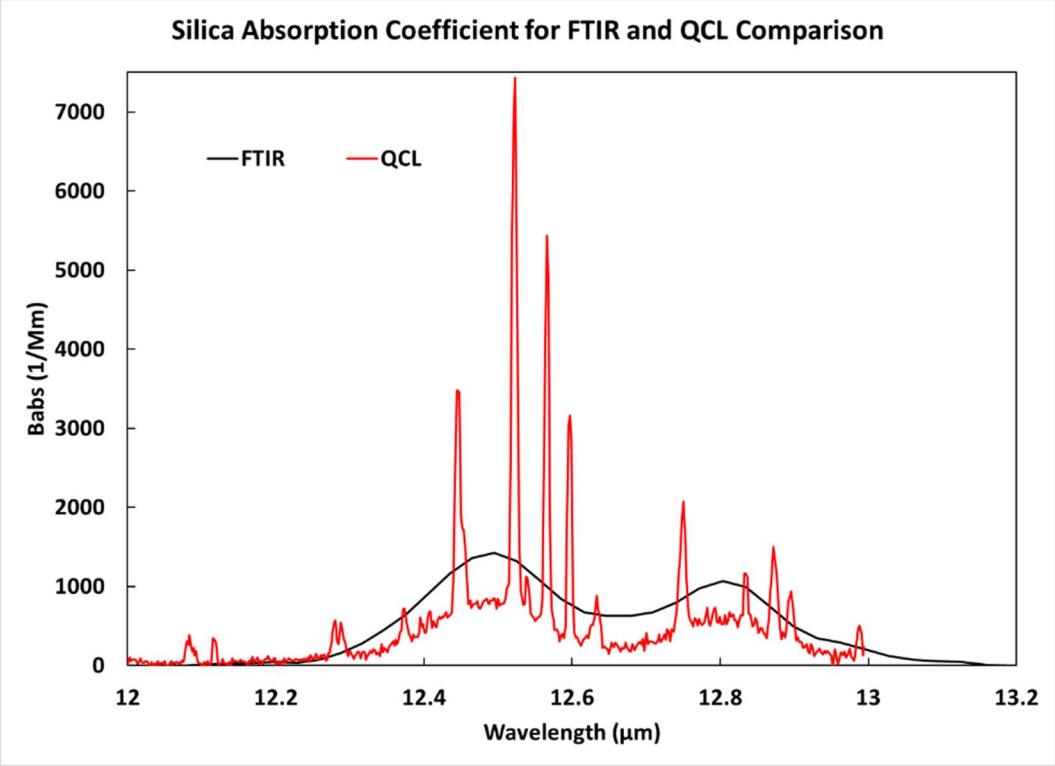

Figure 24: Silica Absorption Coefficient Spectra.

Figure 24 is the silica absorption coefficient spectra collected during a dust experiment by the photoacoustic instrument and filter-based FTIR method. The red line represents the absorption coefficient as measured by the photoacoustic instrument. The black line is the absorption coefficient as calculated from the FTIR transmission spectrum of the filter. The large spikes in the photoacoustic spectra are due to absorption by water vapor or carbon dioxide, as discussed in the previous section. There is remarkable agreement between that of the FTIR filter-based method's absorption coefficient spectrum and that of the QCL photoacoustic instrument. Spectra like these shown here are used to identify candidate wavelengths for measuring concentrations of specific mineral types. In this case, the best candidate for measuring silica concentrations would be the wavelength of 12.495 μm, as this value falls between the water vapor lines but near to the top of the silica absorption peak.

4.3 Kaolinite absorption coefficient spectra

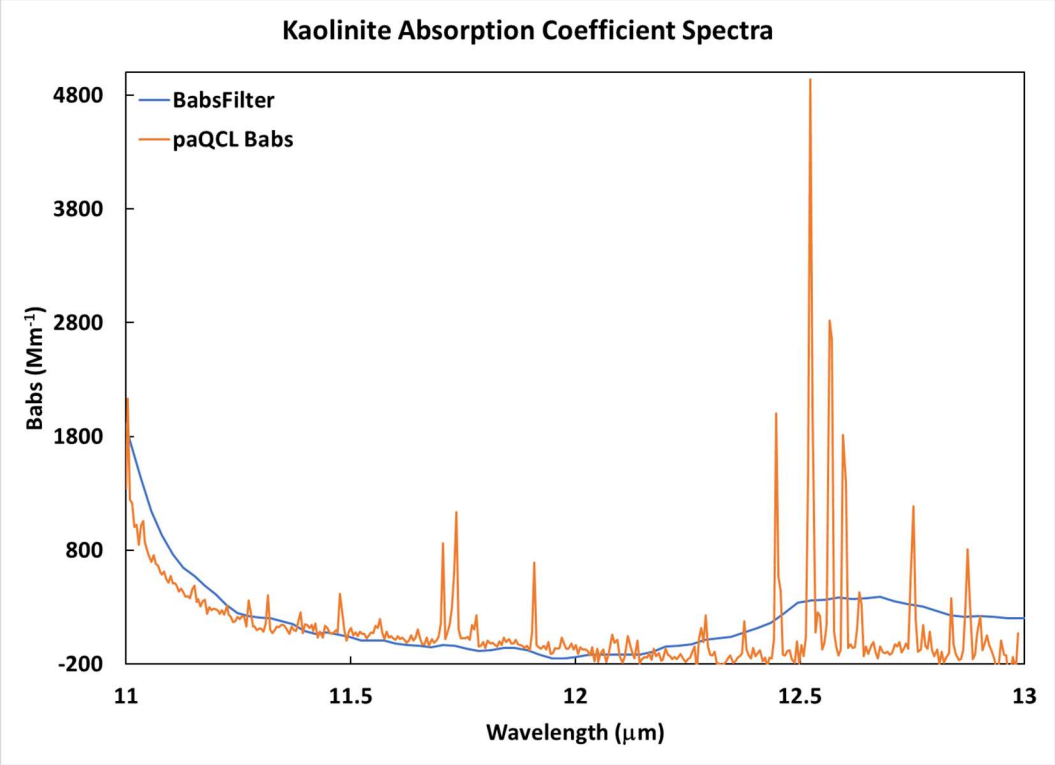

Figure 25: Kaolinite Absorption Coefficient Spectra

As discussed previously, kaolinite is known to be an interferant when attempting to quantify RCS concentrations using current filter-based methods. Because of this, it's important to understand how silica's absorption coefficient spectrum compares to that of kaolinite. Figure 25 demonstrates this. The orange line is the photoacoustic spectrum, and the blue is the FTIR filter-based method spectrum. There are three regions of note for kaolinite in these spectra. On the left side of the graph, the FTIR method and the photoacoustic method match up very well as they climb to a new peak off of the graph.

This region, specifically the wavelength of 11.04 μm, would be a good candidate for quantifying the absorption by kaolinite, since silica does not interfere at this wavelength. The second area of note is the minimal absorption in the spectra around the 12 μm mark. This will be important in section 4.4. The third region of importance is the spectral region that overlaps with silica's region of interest: 12.2 μm to 13 μm. The FTIR method reports that kaolinite is a troublesome interferant when attempting to quantify respirable crystalline silica. This can be seen in Figure 25 with the elevated absorption by kaolinite in this region in the FTIR data. However, the data collected by the photoacoustic instrument reports an absorption coefficient closer to zero for kaolinite in this region, meaning that kaolinite could be a less significant interferant when using the photoacoustic method. This is likely due to drifting of the phase as the instrument scans through wavelengths and should be investigated further to be sure kaolinite is not absorbing more in this region. This will be necessary to understand, as the final purpose of the instrument will be for use in real mining environments, where dust mixtures are unknown and changing all the time. Kaolinite is an incredibly common mineral within the earth's crust, so there is a likelihood that aerosol within mines consists largely of kaolinite. Weak interference by kaolinite in the RCS spectral region would be good news. However, if it could be quantified at 11.04 μm, then it could be accounted for regardless.

4.4 Coal Dust Absorption Coefficient Spectra

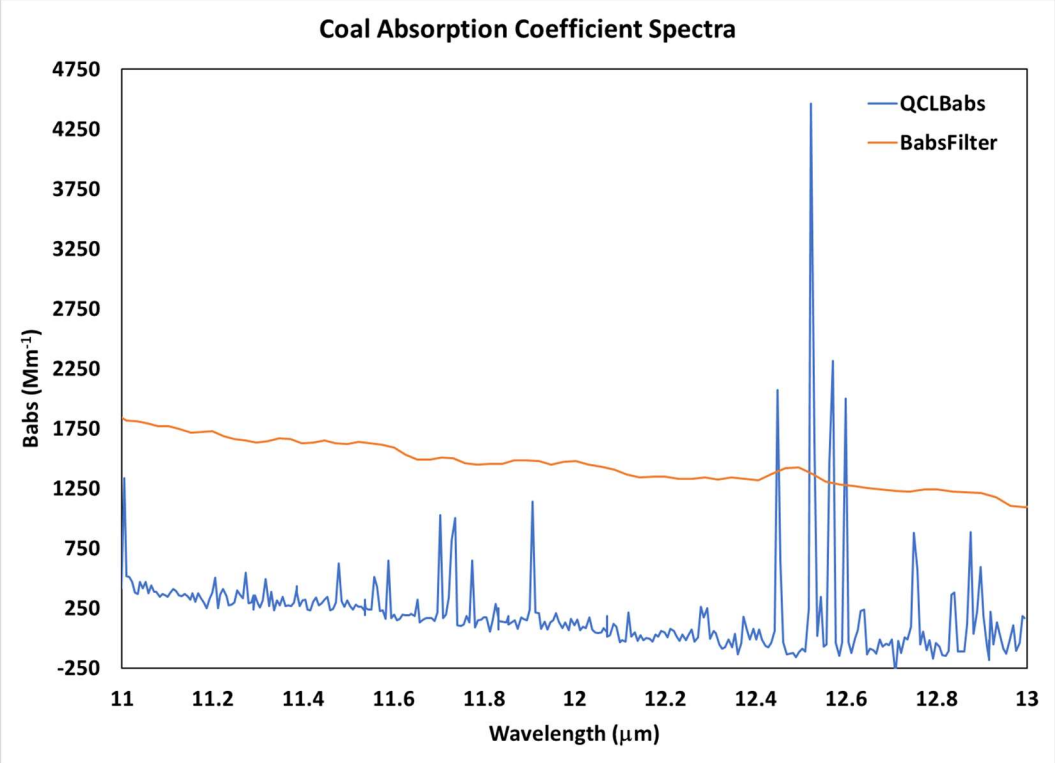

Figure 26: Coal Dust Absorption Coefficient Spectra.

Figure 26 shows the absorption coefficient spectra for coal dust using the photoacoustic method and the NIOSH filter-based method. Because of the dark color of coal, this type of dust tends to absorb light across a very wide spectral range. As shown in Figure 26, the absorption coefficient spectrum for coal tends to be elevated but fairly consistent across the entire spectral range. Again, the photoacoustic method seems to indicate a lower absorption than the filter-based method, as seen previously in kaolinite, with the exception that this applies across the entire range. However, while the

absorption coefficient for coal is low, it is not quite zero, and can therefore still interfere with measurements of RCS and kaolinite. The low absorption of kaolinite around 12 μm, mentioned in the previous section, means that coal dust could be quantified at a similar wavelength without interference by silica or kaolinite.

4.5 SPS30 compared to FAST

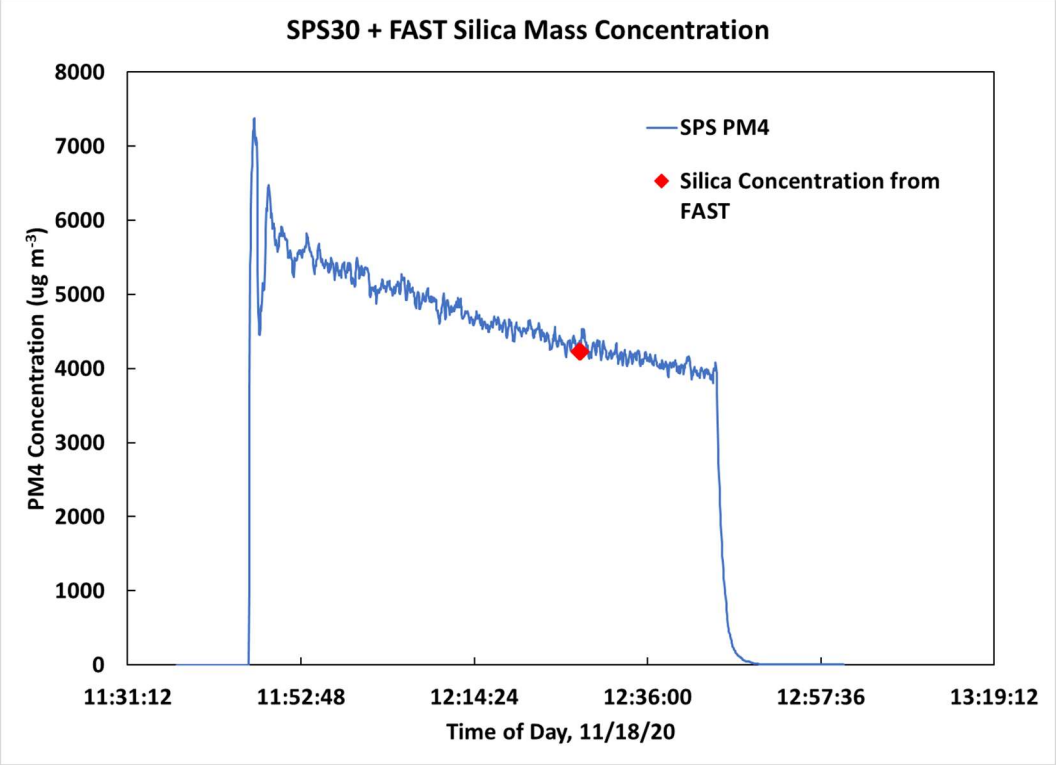

Figure 27: Time Series of SPS30 PM4 and Silica Concentration Obtained from FAST.

As mentioned in section 3.4, the Sensirion SPS30 was used to monitor PM concentrations within the aerosol chamber during experiments. The SPS30 data, in

conjunction with the absorption coefficient data collected by the photoacoustic instrument, can be used to calculate a mass absorbance efficiency for different mineral types at specific wavelengths. However, before this can be done, the SPS30 must be compared against current standards for PM concentration monitoring to determine that the data it reports is reliable. Figure 27 shows a time series of SPS30 PM_4 (blue line) and data acquired from the NIOSH filter-based FTIR technique (red diamond). The NIOSH technique corelates remarkably well with the SPS30. This indicates the SPS30 can be used to calculate an MAE for silica, allowing for the conversion between the absorption coefficient reported by the photoacoustic instrument and silica concentrations. Figure 27 is also indicative of the current lack of real-time measurements of silica, as a single data point would represent an entire shift's worth of sampling, whereas the SPS30 represents a real-time method.

4.6 SPS30 compared to APS

Exploration and comparison of the SPS30 to the APS is an ongoing problem with this project. When used originally, the APS had a high degree of agreement with the SPS30 and their PM_4 concentrations. However, there has since been some confusion regarding how the APS operates and outputs data, and newer experiments have revealed potential disagreements. This is discussed further in the appendix.

4.7 Proof-of-Concept Testing

As part of the testing of the photoacoustic instrument, an experiment to see how the instrument would function during normal operation was devised. The experiment consisted of a mixture of three dust types – silica, kaolinite, and coal dust – mixed and disbursed within the aerosol testing chamber. During the operation of the instrument, the laser wavelength was manually changed to 3 specific wavelengths for different time intervals: 12.495 μm for 9 minutes, 11.04 μm for 6 minutes, and 11.826 μm for 3 minutes. The dust types associated with these wavelengths are RCS, kaolinite, and coal, respectively. The reasoning behind these wavelengths is discussed in previous sections. The timing was chosen as a placeholder for how the instrument might operate under normal conditions, with greater time spent on wavelengths of greater interest. It is also important to note that the instrument was acoustically calibrated and zeroed each time the wavelength was changed. If this experiment is effective, a change in wavelength should provide a clear change in absorption coefficient without a substantial increase in signal noise. This would indicate that the photoacoustic instrument is measuring the signal from a different dust type at each wavelength, lending credence to the theory that the instrument can report concentrations for several different types of dust.

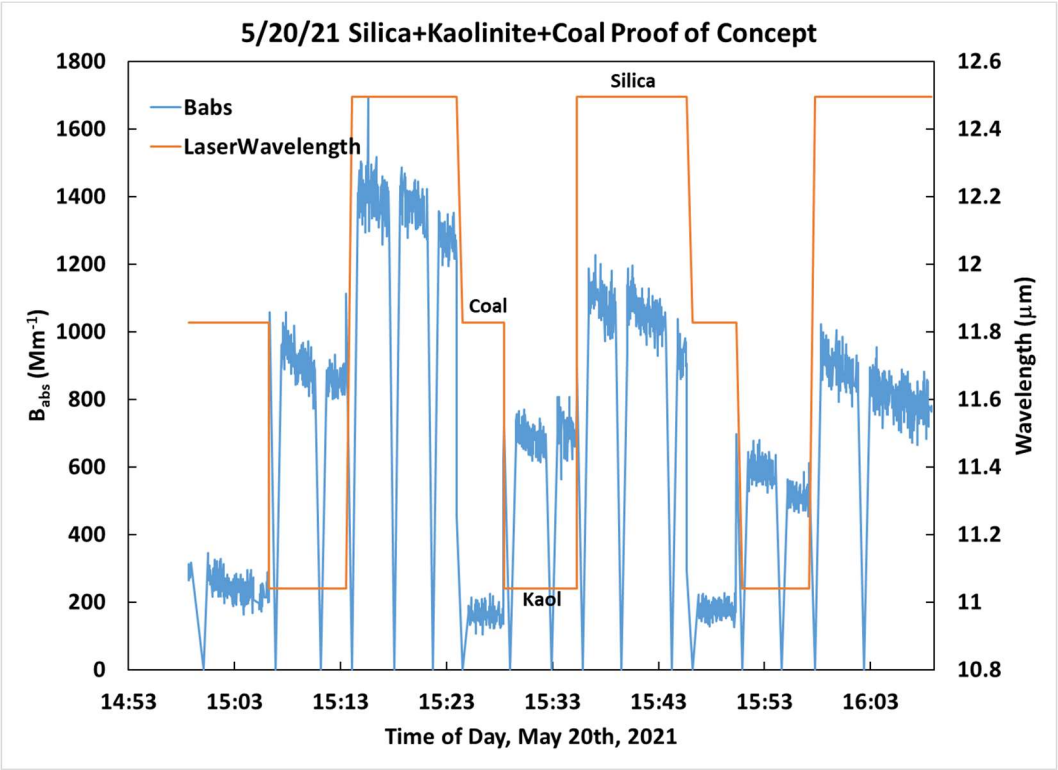

Figure 28: Proof of Concept Time Series.

Figure 28 shows the resulting time series of this test, with the blue line representing the absorption coefficient reported by the photoacoustic instrument and the orange line representing the wavelength of the laser. Each point where the absorption coefficient drops to zero represents a zero calibration being done by the instrument. As expected, with each change in wavelength, the absorption coefficient changes but maintains a good signal.

4.8 Time Series graphs for silica compared to SPS30

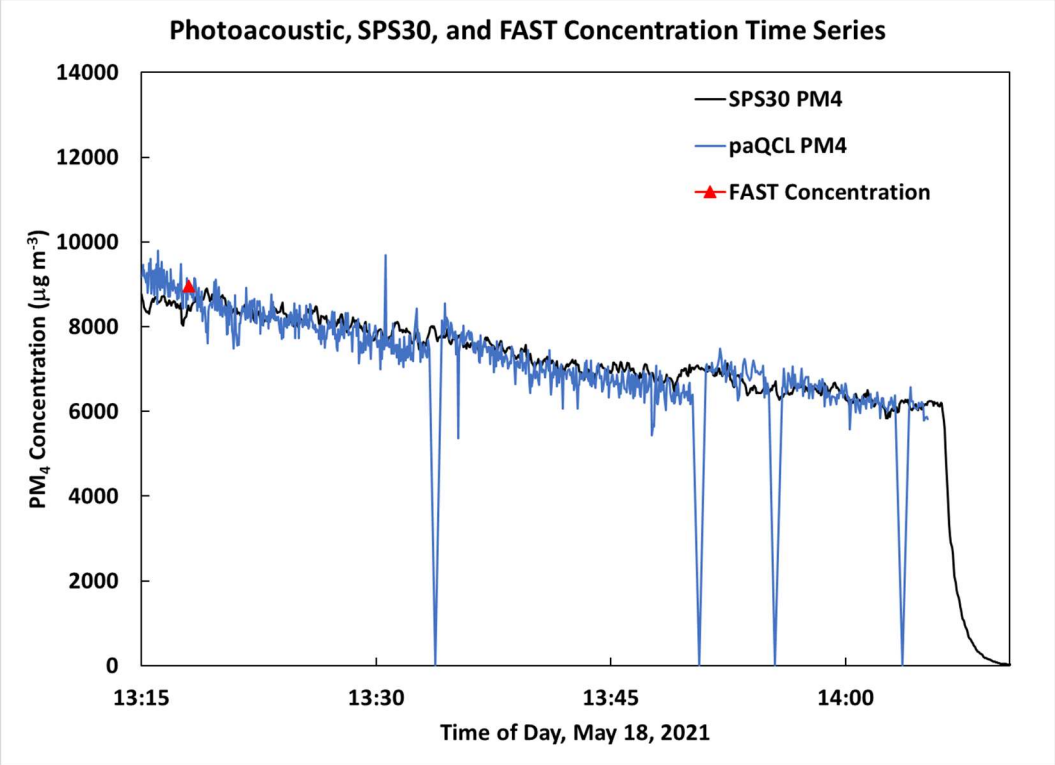

Figure 29: Photoacoustic PM_4 Concentration Compared to SPS30 and FAST Method.

One of the more critical tests is to finally convert the photoacoustic absorption coefficient data into a more usable and relatable quantity: PM_4 concentration. By using the PM_4 concentration data obtained from an SPS30 during a silica monitoring experiment, an MAE can be calculated and used to convert the absorption coefficient. In the case of the above Figure 29, an MAE of 0.246 $m^2\ g^{-1}$ was used achieve this conversion. This value is a bit different compared to the predicted, theoretical MAE of 0.45 $m^2\ g^{-1}$

shown in Figure 13. This can likely be attributed to the prediction's assumption of the small particle limit, which would not be applicable in an experimental setting such as this.

Chapter 5: Conclusions

5.1 Photoacoustic Instrument Capabilities

As discussed in sections 4.2 and 4.8, the photoacoustic instrument is quite capable of measuring and quantifying airborne silica concentrations in real-time. Not only this, but sections 4.3, 4.4, and 4.7 also make note that the instrument is capable of accounting for kaolinite and coal dust as interferants and can even quantify them. This represents a large step forward in silica monitoring technology and dust monitoring in general. The instrument is also capable of self-calibration by use of the water vapor lines present in the mid-infrared spectral range.

5.2 SPS30, FTIR, and APS Agreement

The SPS30 and NIOSH FTIR technique agree very well with one another regarding the concentration of silica during the experiments. This is a good sign, as it means the SPS30 is a strong candidate for use in calculating mass absorbance efficiencies for the different dust types, like kaolinite, that have a similar size distribution and refractive index at visible wavelengths to RCS. These MAEs can in turn be used to convert the photoacoustic absorption coefficients into particulate matter concentrations for those specific dust types. Additional testing needs to be done to verify this further.

The comparison with the APS has been less conclusive and has raised additional questions throughout this investigation. This is addressed further in the appendix.

5.3 Future Work

The photoacoustic instrument represents a substantial step forward in dust monitoring as it provides a real-time alternative to filter-based methods. However, there is still much work that needs to be done on this project. The NIOSH funding of the project is for a personal sampling device, which means the instrument needs to be shrunk down fairly substantially before it can be used as such. In this spirit, the primary concerns would be to decrease the resonator size, find an alternative to the currently used liquid-nitrogen-cooled photodetector, and do some general space and weight optimization regarding the internal aerosol piping and electrical systems of the instrument. A dedicated circuit board needs to be created to replace the breadboarded operational amplifier circuit as well.

In addition to general size optimization, the resonator could be redesigned to be suitable for a 500Hz resonance frequency. This would allow for a longer acoustic period so the thermal relaxation time for the aerosol particles is less of an issue. Use of Helmholtz resonators might be useful to accomplish this.

While the tunable quantum cascade laser has been a crucial part of this research, now that the critical wavelengths have been identified, its use as part of a commercial

version of the instrument becomes questionable. Theoretically, it could be replaced by 3 single wavelength lasers at 12.495 μm, 11.04 μm, and 11.826 μm. Not only would this likely bring the cost of the instrument down, but the individual lasers might be able to provide higher power output than the tunable laser, resulting in greater sensitivity. This could also potentially reduce the need for active cooling of the laser. However, this still needs to be explored.

Finally, the full photoacoustic system needs to be tested at a mine site in the future. This will likely not happen until the instrument is nearer to completion and is deemed safe enough for use in an underground environment.

Works Cited

Arnott, W. P., Hamasha, K., Moosmuller, H., Sheridan, P. J., & Ogren, J. A. (2005). Towards aerosol light-absorption measurements with a 7-wavelength Aethalometer: Evaluation with a photoacoustic instrument and 3-wavelength nephelometer. *Aerosol Science and Technology, 39*(1), 17-29. doi:10.1080/027868290901972

Arnott, W. P., Moosmuller, H., Rogers, C. F., Jin, T. F., & Bruch, R. (1999). Photoacoustic spectrometer for measuring light absorption by aerosol: instrument description. *Atmospheric Environment, 33*(17), 2845-2852.

Arnott, W. P., Moosmuller, H., & Walker, J. W. (2000). Nitrogen dioxide and kerosene-flame soot calibration of photoacoustic instruments for measurement of light absorption by aerosols. *Review of Scientific Instruments, 71*(12), 4545-4552. doi:10.1063/1.1322585

Capasso, F., Faist, J., Sirtori, C., & Cho, A. Y. (1997). Infrared (4-11 mu m) quantum cascade lasers. *Solid State Communications, 102*(2-3), 231-236. doi:10.1016/s0038-1098(96)00711-9

Curl, R. F., Capasso, F., Gmachl, C., Kosterev, A. A., McManus, B., Lewicki, R., . . . Tittel, F. K. (2010). Quantum cascade lasers in chemical physics. *Chemical Physics Letters, 487*(1-3), 1-18. doi:10.1016/j.cplett.2009.12.073

Di Biagio, C., Boucher, H., Caquineau, S., Chevaillier, S., Cuesta, J., & Formenti, P. (2014). Variability of the infrared complex refractive index of African mineral dust: experimental estimation and implications for radiative transfer and satellite remote sensing. *Atmospheric Chemistry and Physics, 14*(20), 11093-11116. doi:10.5194/acp-14-11093-2014

Foster, P. J., & Howarth, C. R. (1968). OPTICAL CONSTANTS OF CARBONS AND COALS IN INFRARED. *Carbon, 6*(5), 719-&. doi:10.1016/0008-6223(68)90016-x

Gerrity, T. R., Garrard, C. S., & Yeates, D. B. (1983). A mathematical model of particle retention in the air-spaces of human lungs. *Br J Ind Med, 40*(2), 121-130.

Glotch, T. D., Rossman, G. R., & Aharonson, O. (2007). Mid-infrared (5-100 mu m) reflectance spectra and optical constants of ten phyllosilicate minerals. *Icarus, 192*(2), 605-622. doi:10.1016/j.icarus.2007.07.002

Grzela, T. (2015). Comparative STM-based study of thermal evolution of Co and Ni germanide nanostructures on Ge(001).

Gyawali, M., Arnott, W. P., Zaveri, R. A., Song, C., Moosmuller, H., Liu, L., . . . Chow, J. C. (2012). Photoacoustic optical properties at UV, VIS, and near IR wavelengths for laboratory

generated and winter time ambient urban aerosols. *Atmospheric Chemistry and Physics, 12*(5), 2587-2601. doi:10.5194/acp-12-2587-2012

Harris, D., McMurry, T., & Caughron, A. (2021). Characterization of Mental Illness Among US Coal Miners. *JAMA Netw Open*. doi:10.1001/jamanetworkopen.2021.11110

Hart, J. F., Autenrieth, D. A., Cauda, E., Chubb, L., Spear, T. M., Wock, S., & Rosenthal, S. (2018). A comparison of respirable crystalline silica concentration measurements using a direct-on-filter Fourier transform infrared (FT-IR) transmission method vs. a traditional laboratory X-ray diffraction method. *Journal of Occupational and Environmental Hygiene, 15*(10), 743-754. doi:10.1080/15459624.2018.1495334

Lewis, K., Arnott, W. P., Moosmuller, H., & Wold, C. E. (2008). Strong spectral variation of biomass smoke light absorption and single scattering albedo observed with a novel dual-wavelength photoacoustic instrument. *Journal of Geophysical Research-Atmospheres, 113*(D16), 14. doi:10.1029/2007jd009699

Lewis, K. A., Arnott, W. P., Moosmuller, H., Chakrabarty, R. K., Carrico, C. M., Kreidenweis, S. M., . . . Mishchenko, M. I. (2009). Reduction in biomass burning aerosol light absorption upon humidification: roles of inorganically-induced hygroscopicity, particle collapse, and photoacoustic heat and mass transfer. *Atmospheric Chemistry and Physics, 9*(22), 8949-8966. doi:10.5194/acp-9-8949-2009

Marple, V. A., & Rubow, K. L. (1983). AN AEROSOL CHAMBER FOR INSTRUMENT EVALUATION AND CALIBRATION. *American Industrial Hygiene Association Journal, 44*(5), 361-367. doi:10.1080/15298668391404978

Miller, A. L., Weakley, A. T., Griffiths, P. R., Cauda, E. G., & Bayman, S. (2017). Direct-on-Filter alpha-Quartz Estimation in Respirable Coal Mine Dust Using Transmission Fourier Transform Infrared Spectrometry and Partial Least Squares Regression. *Applied Spectroscopy, 71*(5), 1014-1024. doi:10.1177/0003702816666288

Moosmuller, H., Chakrabarty, R. K., & Arnott, W. P. (2009). Aerosol light absorption and its measurement: A review. *Journal of Quantitative Spectroscopy & Radiative Transfer, 110*(11), 844-878. doi:10.1016/j.jqsrt.2009.02.035

MSHA. (2010). *Coal Mine Dust Sampling Devices; High-Voltage Continuous Mining Machine Standard for Underground Coal Mines; Final Rules, 75 FR 17511*.

MSHA. (2014). *Lowering Miners' Exposure to Respirable Coal Mine Dust, Including Continuous Personal Dust Monitors; Final Rule, 79 FR 24813*.

Namjou, K., Cai, S., Whittaker, E. A., Faist, J., Gmachl, C., Capasso, F., . . . Cho, A. Y. (1998). Sensitive absorption spectroscopy with a room-temperature distributed-feedback quantum-cascade laser. *Optics Letters, 23*(3), 219-221. doi:10.1364/ol.23.000219

Nascimento, P., Taylor, S., Arnott, W., Kocsis, k., Wang, X., & Firouzkouhi, H. (2021). *Development of a Real Time Respirable Coal Dust and Silica Dust Monitoring Instrument Based on Photoacoustic Spectroscopy*. Paper presented at the 18th North American Mine Ventilation Symposium, Virtual.

NIOSH. (2011). *Current Intelligence Bulletin 64: Coal Mine Dust Exposures and Associated Health Outcomes*.

NIOSH. (2020). NIOSH Field Analysis of Silica Tool Manual. In: NIOSH.

Pampena, J. D., Cauda, E. G., Chubb, L. G., & Meadows, J. J. (2020). Use of the Field-Based Silica Monitoring Technique in a Coal Mine: A Case Study. *Mining Metallurgy & Exploration, 37*(2), 717-726. doi:10.1007/s42461-019-00161-0

Reynolds, K., & Jerome, J. (2021). Silicosis. In (Vol. 69, pp. 51): Sage Publishing.

Rouxel, J., Coutard, J. G., Gidon, S., Lartigue, O., Nicoletti, S., Parvitte, B., . . . Gliere, A. (2016). Miniaturized differential Helmholtz resonators for photoacoustic trace gas detection. *Sensors and Actuators B-Chemical, 236*, 1104-1110. doi:10.1016/j.snb.2016.06.074

Sensirion. (2020). SPS30 Specification Statement. In: Sensirion.

TSI. (2013). Aerodynamic Particle Sizer Spectrometer Model 3321 User's Manual. In (Revision H ed.). www.TSI.com: TSI.

Wei, S. J., Kulkarni, P., Ashley, K., & Zheng, L. N. (2017). Measurement of Crystalline Silica Aerosol Using Quantum Cascade Laser-Based Infrared Spectroscopy. *Scientific Reports, 7*, 8. doi:10.1038/s41598-017-14363-3

Zeidler, S., Posch, T., & Mutschke, H. (2013). Optical constants of refractory oxides at high temperatures Mid-infrared properties of corundum, spinel, and alpha-quartz, potential carriers of the 13 mu m feature. *Astronomy & Astrophysics, 553*, 15. doi:10.1051/0004-6361/201220459

Appendix

As mentioned previously, the SPS30 and APS comparisons have been an ongoing investigation within this project and have begun to move beyond the scope of this thesis. During our first experiments, after spending time learning about the instrument and graphing the data, we found that the APS PM_4 tended to agree with the SPS30 PM_4 quite well, as shown in Figure 30. The data was exported via the AIM software with a density of 1 g cc^{-1}, and then was multiplied by a density of 2.2 g cc^{-1}.

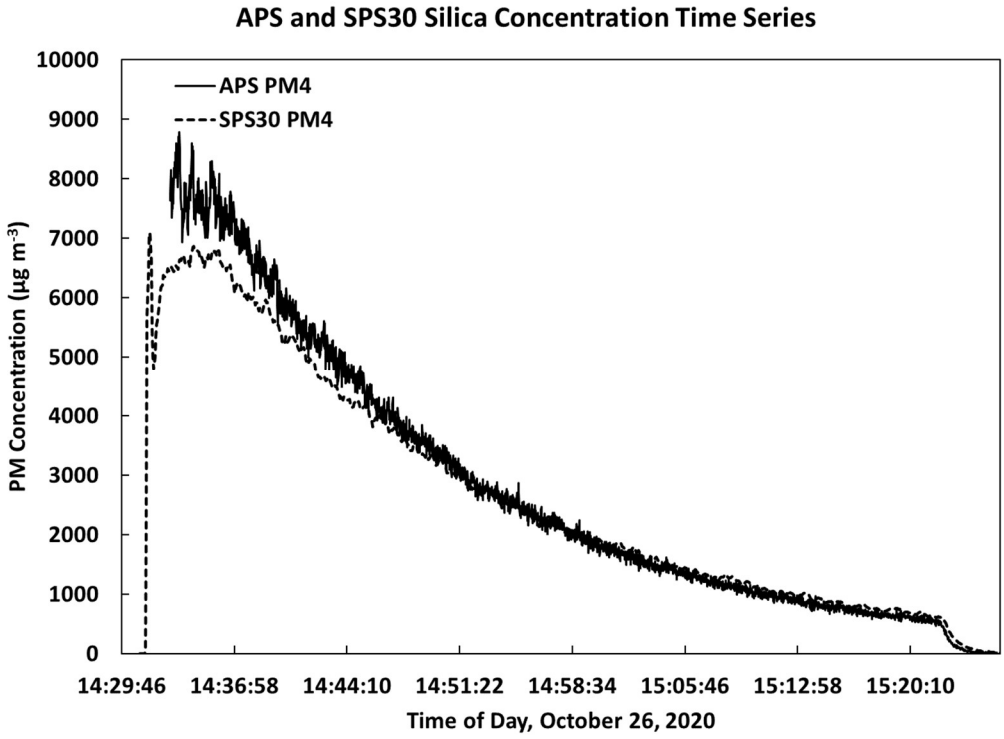

Figure 30: The first comparison of APS and SPS30 shows good agreement between the instruments.

While the agreement of these two instruments would be a very good thing for this project, there has been some question as to how the APS is operated and whether the concentrations matching was a coincidence or not. Upon further investigation and use of the APS, the SPS30 and APS were found to instead be in disagreement, with the SPS30 typically measuring concentrations about 3 times higher than the APS. This is shown in Figure 31.

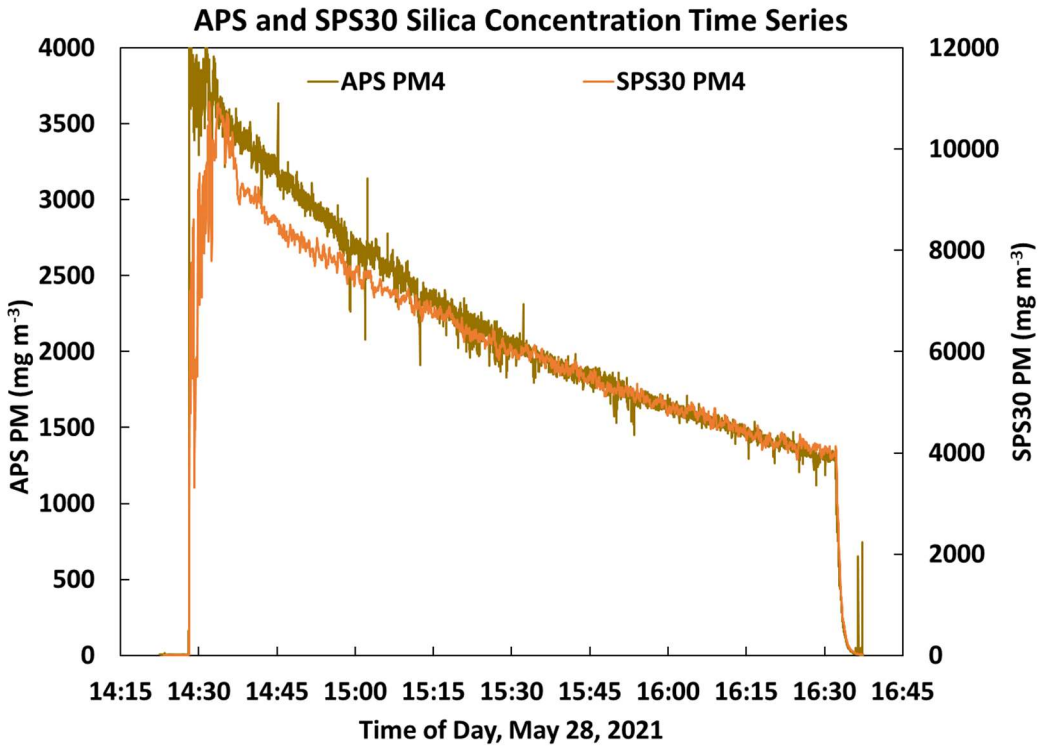

Figure 31: An additional test between the SPS30 and APS showcasing the disparity between the two.

The cause for this new extreme difference between the two instruments is likely a result of a few things. First, AIM, the software that handles data exporting and sampling control

for the APS, has several different methods for manipulating and exporting data. There have been some inconsistencies discovered in our files regarding this. Additionally, the APS was originally operated with a diluter, which has not been used in more recent experiments. The diluter allows the sample intake of the instrument to be controlled so that the APS is not inundated with particles while sampling at high concentrations. During the course of this project, experiments with the photoacoustic instrument and SPS30 have typically been done at very high PM concentrations, which would negatively affect the ability of the APS to accurately count and size particles if a diluter is not used. This has likely caused a large part of our misunderstanding of the instrument and should be investigated further.

As it stands now, the data collected using the APS is suspect. The APS data would be a valuable addition to the study. Future work is already being discussed regarding how to proceed with this. Depending on the results, this could greatly improve the standing of the photoacoustic instrument in its ability to measure mineral dust concentrations.